# Facies associations, detrital clay grain coats and mineralogical characterization of the Gironde estuary tidal bars: A modern analogue for deeply buried estuarine sandstone reservoirs

Maxime Virolle, Hugues Féniès, Benjamin Brigaud, Raphaël Bourillot, Eric Portier, Patricia Patrier, Daniel Beaufort, Isabel Jalon-Rojas, Hervé Derriennic, Serge Miska

## To cite this version:

Maxime Virolle, Hugues Féniès, Benjamin Brigaud, Raphaël Bourillot, Eric Portier, et al.. Facies associations, detrital clay grain coats and mineralogical characterization of the Gironde estuary tidal bars: A modern analogue for deeply buried estuarine sandstone reservoirs. Marine and Petroleum Geology, 2020, 114, pp.104225 (IF 3,538). 10.1016/j.marpetgeo.2020.104225 . hal-02447126

**HAL Id: hal-02447126**
**https://hal.science/hal-02447126**

Submitted on 21 Jul 2022

# Facies associations, detrital clay grain coats and mineralogical characterization of the Gironde estuary tidal bars. A modern analogue for deeply buried estuarine sandstone reservoirs.

Maxime Virolle[1], Hugues Féniès[2], Benjamin Brigaud[1], Raphaël Bourillot[2], Eric Portier[3], Patricia Patrier[4], Daniel Beaufort[4], Isabel Jalon-Rojas[5], Hervé Derriennic[6], Serge Miska[1]

[1]Université Paris-Saclay, CNRS, GEOPS, 91405 Orsay, France
[2]Géoressources et Environnement, ENSEGID, Bordeaux INP, Université Bordeaux Montaigne 33607 Pessac, France
[3]Neptune Energy, 9-11 Allée de l'Arche, 92400 Courbevoie, France
[4]Univ. Poitiers, IC2MP, CNRS, UMR 7285, TSA 51106 86073 Poitiers Cedex 9, France
[5]The Sino-Australian Research Centre for Coastal Management, School of Physical, Environmental and Mathematical Sciences, UNSW Canberra, Canberra, Australia
[6]EPOC-OASU, CNRS, Université de Bordeaux, Site de Talence, Bâtiment B18N, 33615 Pessac Cedex

Corresponding author: maxime.virolle@u-psud.fr, GEOPS, Univ. Paris-Sud, CNRS, Université Paris-Saclay, 91405 Orsay, France

Short title: Multi-scale tidal bars characterization

# Abstract

Estuarine tidal bar sandstones are complex reservoir geobodies commonly exploited by the oil and gas industry. In order to better predict the reservoir potential of these geobodies, this study provides a modern-day reservoir analogue, describing tidal bars in the inner and outer Gironde estuary from the microscopic to the macroscopic scale.

The originality of this work lies in the multi-scale study of modern estuarine tidal bars based on numerous piston cores extracted in a high-energy environment. This work demonstrates that these tidal bars are composite sedimentary bodies made up of individual reservoir sand units separated by thick muddy layers. Their vertical facies associations and internal architectures are controlled by local hydrodynamic variations and seasonal river influxes. Detrital clay grain coats are notably characterized using a portable and handheld mineral spectrometer from the base to the top of the tidal bars. X-ray diffraction and electron microscopes reveal that these coats are mainly composed of di-octahedral smectite, illite, chlorite and kaolinite associated with other components such as diatoms or pyrite. The best reservoir geobodies are those with the minimum clay permeability barriers at the macro and mesoscale. An optimum coated grain content and clay fraction volume is also needed for generating authigenic clay coatings and inhibiting quartz overgrowth. These conditions are met within the tidal sand bars of the outer estuary funnel that are expected to be the best reservoir geobodies in deeply buried sandstones.

Keywords: Tidal bars, hydrodynamic, coats, clay, reservoir.

## 1. Introduction

Estuarine sandstone geobodies are characterized by their internal architecture, which is highly variable and complex, both laterally and vertically (Olariu et al., 2012; Taylor et al., 2015). The successive deposition of clay-rich and sand-rich layers, as a consequence of temporal and spatial variations in tidal currents, influence their architecture (Reineck and Wunderlich, 1968; Visser, 1980; Dalrymple et al., 1991; Yoshida et al., 1999; Martinius et al., 2005; Massart, 2014). Tidal bars and heterolithic point bars deposited within estuaries display a multi-scale architecture and heterogeneity due to the succession of clay-rich and sand-rich layers (Féniès and Tastet, 1998; Tessier et al., 2012; Chaumillon et al., 2013; Shchepetkina et al., 2016). Within estuarine sandstones reservoirs, these heterogeneities will exert a key control on the flow of gas, oil and water during field production (Weber, 1986; Jackson et al., 2005, 2003; Ringrose et al., 2005; Nordahl et al., 2005, 2006; Nordahl and Ringrose, 2008).

The aggregation of clay particles and sand grains generates micrometre scale (pore scale) heterogeneity within estuarine sand bars. Clay minerals may fill porosity but may also form coats around sand grains that will influence physical properties in buried sandstone reservoirs (Bloch et al., 2002; Wooldridge et al., 2017; Stricker and Jones, 2018). Previous studies showed that chlorite coatings may inhibit quartz overgrowth nucleation, one of the main porosity reduction mechanism, and thereby preserve reservoir quality at great depth (Ehrenberg, 1989; Houseknecht and Pittman, 1992; Bjorlykke and Egeberg, 1993; Ehrenberg, 1993; Aase et al., 1996; Bloch et al., 2002; Storvoll et al., 2002; Bjørlykke, 2014). The formation of these coatings may originate from transformations of clay mineral precursors (e.g. berthierine or odinite; Worden and Morad, 2003; Gould et al., 2010; Beaufort et al., 2015). Detrital clay grain coats formed within estuarine deposits can initiate chloritization by supplying the detrital material necessary to form the precursors (Beaufort et al., 2015; Griffiths et al., 2018, 2019a; Virolle et al., 2019). Exopolymeric substances (EPS) produced by diatoms may have a key role in binding clay particles around sand grains that are probably coated just before deposition within sand dunes (Jones, 2017; Virolle et al., 2019). Besides, primary depositional mineralogy (quartz, feldspars, carbonates and clay minerals) distribution also influence sandstone reservoir quality (Griffiths et al., 2019b). However, only few studies have analysed detrital clay grain coats and detrital minerals distribution in surface or sub-surface estuarine sediments (Shchepetkina et al., 2016; Wooldridge et al., 2017; Griffiths et al., 2018; Shchepetkina et al., 2018; Virolle et al., 2019). The Ravenglass Estuary, the Petitcodiac River, the Ogeechee River estuary and the Gironde are among the rare examples of high resolution study that investigate both surface and subsurface sediment in terms of clay coat, clay mineral and coarse-fraction mineralogy (Wooldridge et al., 2017; Griffiths et al., 2018, 2019a, 2019b).

Understanding the processes at the origin of multi-scale reservoir heterogeneities is a key scientific challenge for better predicting reservoir quality distribution at great depth. To do so, the best way remains studies of modern sedimentary analogues, of outcrops and of drill core (Wood, 2004; Musial et al., 2012; Olariu et al., 2012; Saïag et al., 2016; Aschoff et al., 2018)

In this study, we investigate tidal sand bars from the Gironde Estuary, which may be considered as a modern analogue of many ancient tidal bars (Allen, 1991). The Gironde estuary is a mud-rich, macrotidal estuary with heterolithic point bars and tidal bars up to several kilometres long, making them comparable in size to ancient estuarine reservoir geobodies, such as the Permian Cape Hay Formation (Bonaparte Basin, Australia; Saïag et al., 2016), the Early Cretaceous Sego Formation (Colorado, United States; Aschoff et al., 2018) or the Cretaceous McMurray Formation (Alberta, Canada; Musial et al., 2012). Elongate tidal bars present both lateral and longitudinal accretion surfaces (Féniès and Tastet, 1998; Olariu et al., 2012; Chaumillon et al., 2013; Legler et al., 2013). The Gironde estuary is also characterized by a well-developed Turbidity Maximum Zone (TMZ), which allows the deposition of clay-rich layers within tidal bars (Allen, 1991; Féniès et al., 1999 ; Doxaran et al., 2009; Jalón-Rojas et al., 2015). Although many sedimentological studies have been carried out on the estuary, the relationship between hydrodynamics, vertical facies associations and the distribution of detrital clay grain coats and clay minerals remains poorly understood.

This paper presents the investigation of sediment cores drilled from two tidal bars located 40 km apart in the Gironde estuary: the Plassac tidal bar, in the inner estuary funnel, and the Richard tidal bar, in the outer estuary funnel. Six 4.5 to 6.70 m long cores were extracted, three from each bar. Studies were conducted at the pore scale (micrometres), the facies association scale (metres), up to the reservoir architecture scale (hundreds of metres to several kilometres). Grain size, clay fraction content (< 2 µm) and assemblage, coated grain abundance (percentage of grains with clay attached to their surfaces) and coat coverage were analysed from cores samples. A portable and handheld mineral spectrometer was used to test its robustness to characterize clays in sands. The facies and mineralogy described in this study may be useful for geologists describing detrital cores.

Specific research questions will be addressed:

- Do clay coats exist at several meters depth in modern tidal bars subjected to strong hydrodynamics? How are clay coats distributed in near surface estuarine sediments (<10m)? What processes controlled their formation and distribution?

- How are clay minerals distributed with depth and along the estuary?
- What are the processes governing the multi-scale heterogeneities within estuarine tidal bars? Is that possible to predict which depositional environments will have the best reservoir quality after burial?

# 2. Study area: Gironde estuary

## 2.1. Morphological settings and studied sites

The Gironde estuary is located in south-western France begins (Fig. 1). It is a worldwide reference model for mixed tide- and-wave-dominated incised valleys (Allen and Posamentier, 1994; Lericolais et al., 1998, Féniès et al., 2010). The estuary is divided into three morphological zones, comprising from upstream to downstream: (1) the Garonne and Dordogne estuarine meandering channels, characterized by the deposition of heterolithic point bars, (2) the inner estuary funnel, including the tidal bars of the bay-head delta, and (3) the outer estuary funnel, consisting in a wide muddy central basin with tidal bars and a large tidal inlet at its seaward extremity (Fig. 1: Allen, 1991 ; Virolle et al., 2019).

Two tidal bars have been studied in the Gironde during recent decades: (1) The Plassac tidal bar (Billy et al., 2012; Chaumillon et al., 2013), at the landward extremity of the bay-head delta, 65 km inland from the estuary mouth and (2) the Trompeloup tidal bar (Féniès et al., 1998), at the seaward extremity of the bay-head delta, 45 km inland from the estuary mouth. These tidal bars belong to the bay-head delta that extends from 75 to 35 km inland from the estuary mouth (Fig. 1). Fluvial sands deposited in the estuary funnel during the last

4000 years compose these tidal bars that are part of the Highstand Systems Tract (HST), which is gradually filling the Gironde Estuary funnel (Allen, 1991; Allen and Posamentier, 1994).

This study focuses on two tidal bars located 40 km apart (Fig. 1): (1) the Plassac tidal bar, which is 4.6 km long and 1.4 km wide and located in the inner estuary funnel (described above), from which three new cores were collected and (2) the Richard tidal bar, in the outer estuary funnel, 25 km from the estuary mouth, from which another set of three cores was collected. This sandy tidal bar is about 4 km long and 300 m wide and has been deposited between tidal channels. Both tidal bars were chosen as they are well preserved, well-developed and remain accessible for coring.

## 2.2. Hydrodynamics of the Gironde estuary

In the Gironde, tides are semi-diurnal, and the estuary is macro-tidal (Allen, 1972). Tidal range between 2.5 and 5m on mean neap/spring tides at the estuary mouth (Bonneton et al., 2015). As tidal wave migrates upstream, both tidal amplitude and asymmetric shape of the wave are amplified (Jalon-Rojas et al., 2018). The Gironde estuary is therefore defined as a hypersynchronous estuary (Allen, 1991). At the upstream tidal current limit (160 km from the estuary mouth during the low-river stage), the tidal range and tidal-current velocities fall to zero (Allen, 1972; Allen et al., 1980).

For both tidal bars located in the estuary funnel, the ebb flow is the faster current (Allen, 1972; Castaing, 1981; Féniès et al., 1999). For example, Féniès et al. (1999) measured maximum ebb velocity of 80 $cm.s^{-1}$ and maximum flood velocity of 52 $cm.s^{-1}$ during spring tides in the intertidal zone of the Plassac tidal bar. In the subtidal zone, tidal velocities can reach 200 $cm.s^{-1}$ and are still ebb dominated (Castaing, 1981).

The estuary is also characterized by a well-developed Turbidity Maximum Zone (TMZ) with Suspended Particle Matter (SPM) concentration that varies between 1-10 g.l-1 in the estuarine waters (Allen, 1972; Allen et al., 1977, 1980; Sottolichio et al., 2011; Savoye et al., 2012). This high turbidity zone has a major effect on sedimentation processes (Allen, 1972, Sottolichio et al., 2011). The TMZ position varies seasonally in the estuary with fluvial discharge (Allen, 1972).

# 3. Material and methods

## 3.1. Coring

The originality of this study lies in the core dataset sampled from two tidal bars, the Plassac bar in the inner estuary and the Richard tidal bar in the outer estuary. Six campaigns were carried out to extract cores from the tidal bars. Three cores were sampled from each bar along East–West transects perpendicular to the long axis of the bars (North–South). On the Plassac tidal bar (45°06’24.49’’N 0°39’37.87’’W), the three campaigns took place on 23–26 November 2015. Three cores, named PLA-2015-East, PLA-2015-Centre and PLA-2015-West were collected with a core spacing of about 150 m. The core lengths vary from 4.44 m to 6.70 m. On the Richard tidal bar (45°26’19.18’’N 0°54’37.81’’W), the first core (Ri-2016-C) was extracted on 21 April 2016, and the other two on 19–20 October 2016 (Ri-2016-E and Ri-2016-W). Extraction was made along a 90 m long transect, with a core spacing of about 45 m. The spacing is tighter than at Plassac because the Richard tidal bar is narrower. The core lengths vary from 4.60 m to 6.50 m.

Cores were recovered by using a portable vibro-corer (De Resseguier, 1983). During the coring process, the core barrel is hammed without any rotation and a reference line indicating the ebb direction is marked all along the core section. At the lab, the core is open accordingly to this reference line, which allows distinguishing the orientation of the dune bedding (ebb & flood). The cores were opened and pictured at the "Sediment Archive Analysis" Platform at the EPOC laboratory (Univ. Bordeaux, France). Half of each core was used to describe sedimentary facies while the other half was used for sampling.

### 3.2. Petrography

Fifty-three plugs were sampled from the Plassac cores and 32 plugs from the Richard cores in a manner that prevented strong disturbance of the sedimentary fabric. Thin sections were made and observed in transmitted and reflected light.

As described in Virolle et al. (2019), the relative surface area (%) of the sediment components and the grain coat coverage were quantified. The macroporosity was determined by blue thresholding using Jmicrovision software. In each thin section, the relative surface area (%) of the coated and non-coated grains (quartz, feldspars, lithics, bioclasts, pyrite, micas) and also clay matrix were quantified using random grid point counting with JmicroVision Image analysis software (Roduit, 2007). Following the methodology described by Wooldridge et al. (2017a), the coated grains category was divided into four sub-categories depending on the grain coat coverage of the grain surface: (1) 1–5%, (2) 5–15%, (3) 15–30% and (4) more than 30%. Scanning Electron Microscope (SEM) observations were also realized on individual sand grains. Sediment grain size was analysed on 91 samples using a Mastersizer 2000 laser granulometer (Malvern, Worcestershire, UK). Mean grain size was calculated using Folk's (1980) equation (see Virolle et al., 2019). During the experiment, mud pebbles were disaggregated and were therefore counted as a part of the fine fraction (<2 µm).

## 3.3. Mineralogy

As “clay” may refer to grain size as well as mineralogy, this study uses the term clay fraction to define the fine-grained fraction less than 2 µm including clay minerals (Grim, 1942). The relative weight percentage of the clay fraction of homogenized sediment subsamples was measured and expressed as a weight percentage of the sample (wt. %; Virolle et al., 2019). The composition of the clay fraction (< 2 µm) of 45 samples was determined by X-ray diffraction (XRD), and semi-quantitative estimations of clay mineral proportions were performed with Macdiff software. For analytical detail, see supplementary data S1.

Short wavelength infrared (SWIR) spectroscopy was performed on 391 samples using a portable and handheld spectrometer (ASDinc TerraSpec4 of PANanalytical): 162 samples from core PLA-2015-E, 175 samples from PLA-2015-W and 54 from Ri-2016-W. Mid-infrared (MIR) spectroscopy was performed on 10 samples from the Plassac tidal bar previously analysed by XRD. Sampling for SWIR was conducted every 2 cm. Analyses were conducted on bulk samples (any fraction combined, while only the fraction < 2 µm was studied in XRD).

Cation exchange capacity (CEC) was measured on eight samples from PLA-2015-W. CEC was expressed in milli-equivalents per 100 g. CEC can be indicative of the proportion of “swelling” clays such as smectite in the sample. The detail of analytical procedure is available in supplementary data S1.

Three samples were also observed under Transmission Electron Microscopy (TEM), on a TECNAI G2 FEI TEM with an acceleration voltage of 200 kV and a spot size of about 5 nm. Most pictures were taken in TEM mode and analyses were performed in STEM (Scanning Transmission Electronic Microscopy) mode. The chemical composition obtained in oxide weight percentage (wt %) was converted into atomic percentage to estimate the structural formulas. Then, calculated atomic concentrations were plotted in the ternary diagram M+4Si R2+ (Meunier and Velde, 1989) and used to determine intimate clay mixtures.

### 3.4. Datings

Large organic matter particles (wood fragments, leaves or seeds) were radiocarbon dated. For the Plassac tidal bar, the carbon 14 ($^{14}C$) ages were obtained from the accelerator mass spectrometers (AMS) at the Adam Mickiewicz University in Poznań (Goslar et al., 2004) from 14 samples. For the Richard tidal bar, the graphite sources were prepared at GEOPS (Univ. Paris-Sud, Orsay, France), and $^{14}C$ counted with the low energy AMS “ECHoMICADAS - Environnement Climat et Homme Micro Carbon Dating System” at LSCE (Université Paris-Saclay/CEA/CNRS, Gif-sur-Yvette, France) on 29 samples. Analytical errors, including laboratory errors, are ± 0.1‰ for $\delta^{13}C$ and between 0.5 and 0.8 pMC (percentage of Modern Carbon) for $^{14}C$ activity. Gibert et al. (2002) provides a complete description of the equipment and protocol.

### 3.5. Hydrologic data

River discharge data monitored by the French Ministry of Ecology and Energy (Hydro database; http://www.hydro.eaufrance.fr) were used to determine seasonal estuary discharge. Estuary discharge is calculated as the sum of discharges from both the Garonne (monitored at Portet-sur-Garonne, upstream of the tidal influence, 43°31'15.39"N and 1°24'8.71"E) and Dordogne (Cenac-et-Saint-Julien, 44°48'15.51"N and 1°12'22.74"E) from 1925 to 1996 using annual mean values. Bathymetric data were obtained from the Bordeaux Harbour Authorities (Grand Port Maritime de Bordeaux).

Additional details concerning material and methods are provided in Appendix S1.

# 4. Results

## 4.1. Facies characterization of the inner to outer estuary funnel tidal bars

The facies descriptions are presented from the base to the top of the cores and are summarized in Table 1 and detailed grain composition in appendix S2. Globally, the vertical facies associations of both tidal bars present coarsening-upward grain-size trends: (i) for the Plassac bar, the average mean grain-size increases from 231 µm at the base to 252 µm at the top; (ii) for the Richard bar, it increases from 183 µm (base) to 213 µm (top). For both tidal bars, samples are composed of quartz (P= 31% and R= 27%), feldspars (P= 7% and R= 4%), lithics (P= 14% and R= 13%), carbonates (P= 3% and R= 6%), clay (P= 16% and R= 10%), pyrite (P= 0.24% and R= 0.5%), and others including micas or heavy minerals (P= 4% and R= 4%). The samples are classified into litharenite to feldspathic litharenite in the Folk diagram (Fig. 2). Porosity values are higher in the Richard tidal bar (*ca*. 35%) than within the Plassac tidal bar samples (*ca*. 25%).

The bottom of both tidal bars is composed of the Fluid mud facies (F1). This facies is only observed on the Ri-2016-W core. In the Plassac tidal bar, it was observed in cores sampled in 2010 (Chaumillon et al., 2013). Millimetre-thick stacked clay drapes, within which groups of sand ripples alternate with groups of linsens in a cyclic pattern, suggesting a neap-spring cycle layering, are observed in the Plassac tidal bar (F1a). In the Richard tidal bar, decimetre-thick homogeneous fluid mud layers composed this facies (F1b). Clay fraction within samples is about 29 wt% (Richard tidal bar, Table 2). Then, tidal bars are composed by the Lower sand bar facies (F2) whose main characteristics are small dunes with abundant centimetre-sized mud pebbles and numerous millimetre thick clay drapes deposited on the dune foresets and bottomsets (Figs 3 and 4; Table 1). Clay drapes and mud pebbles are thicker and more abundant on the Plassac tidal bar. The clay fraction is about 21 wt% for Richard and 25 wt% for Plassac (Table 2). Above, it is the Middle sand bar facies (F3) in the middle part of both tidal bars (Figs 3 and 4; Table 1). This facies is composed by small to medium-sized dunes with rare mud pebbles and thin clay drapes deposited on dune foresets and bottomsets (Figs 3 and 4; Table 1). The clay fraction is *ca.* 14 wt% for Richard and 15 wt% for Plassac (Table 2). Bioclast fragments and foraminifera are observed in thin sections. The middle part of both tidal bars is also composed by the Middle bar muddy facies (F4). In the Plassac tidal bar, it consists of a muddy matrix that exhibits characteristic lenticular bedding with millimetre-thick alternations of very fine-grained silty linsens and slack-water clay drapes (F4a; Fig. 3; Table 1). It was recovered in the Pla-2015-E core only. In the Richard tidal bar, this facies is observed in all three cores (F4b) and also exhibits the characteristic lenticular bedding described above (Fig. 4). The middle part of both tidal bars is covered by the Upper sand bar facies (F5; Figs 3 and 4). Sedimentary structures within both tidal bars are almost identical with small tidal dunes, but the difference is in the preserved clayey sedimentary structures: abundant centimetre-thick mud pebbles and thick clay drapes are deposited on dunes foresets and bottomsets within the Plassac tidal bar (F5a), while rare clay drapes and clay pebbles are deposited within the Richard tidal bar (F5b; Figs 3 and 4; Table 1). The clay fraction is *ca*. 20 wt% in (F5a) while it is *ca*. 17wt% in (F5b; Table 2). Facies (F5) is the last facies observed within the Richard tidal bar (Fig. 4). In the Plassac tidal bar, facies (F5) is capped by the Tidal flat facies (F6) made of flaser, wavy and lenticular bedding (Table 1). Finally, the Tidal marsh facies (F7) is the top of the vertical facies association of the Plassac tidal bar with amalgamated high-tide slack-water clay drapes, organic matter debris and abundant reed roots (Fig. 3; Table 1). Top of the Plassac tidal bar (from F5 to F7) is therefore finning-upward.

## 4.2. Tidal sand bar internal architecture

A reconstruction of the bars' internal architecture is proposed (Fig. 5 for the Plassac tidal bar, and Fig. 6 for the Richard tidal bar).

In the Plassac tidal bar (Fig. 5), the Lower sand bar facies (F2) is laterally continuous between the central and eastern cores (PLA 2015-C, PLA 2015-E), and the western core (PLA 2015-W) was probably not long enough to reach this facies. Above it, the Middle sand bar facies (F3) is a meter-thick laterally continuous layer, which constitutes the bulk of the tidal bar. This facies (F3) is capped by the Upper sand bar facies (F5a) that is also laterally continuous across the tidal bar. On the eastern part of the bar (core PLA 215-E) two layers of the F5a facies are isolated from one another by an eastward dipping layer of the Middle bar muddy facies (F4a). The (F5a) facies is capped by the Tidal flat facies (F6) as observed in the western and middle cores (PLA 2015-W, PLA 2015-C). It thickens westward and dips gently in the same direction. It is noteworthy that the major part of the tidal bar is composed of sandy units (facies F2, F3 and F5a) that are vertically and laterally connected to each other (Fig. 5) and could be considered as a single reservoir cell. The only reservoir heterogeneity is observed on the eastern side of the bar, where a decimetre-thick layer of the Middle bar muddy facies (F4a) isolates two metre-thick layers of the Upper sand bar facies (F5a).

The fourteen radiocarbon ages ($^{14}C$), measured on the three cores (PLA 2015-W, PLA 2015-C, PLA 2015-E) show very heterogeneous ages, ranging from 5230 ±40 years Before Present (BP) to the present. Except for one age (5230 ±40 years BP), all $^{14}C$ ages are younger than

1,000 years BP (Fig. 5). Modern ages and younger than 200 years BP are dominant in the upper part of the tidal bar (Facies F5 and F6, Fig. 6).

In the Richard tidal bar (Fig. 6), the Fluid mud facies (F1b) was encountered at the base of the bar in two cores (Ri-2016 W and Ri-2016-E). The central core (Ri-2016-C) was not long enough to reach this facies. Then, the Lower sand bar facies (F2) and the Middle bar facies (F3) are laterally continuous and thicken westward (Fig. 6). The Middle bar muddy facies (F4b), which caps the (F3) facies, is laterally continuous across the tidal bar. It dips gently (1.5° dip-angle) and thickens eastward. Then, the Upper sand bar facies (F5b) was deposited at the top of the tidal bar on the Middle bar muddy facies (F4b). It is laterally continuous across the bar and it thickens eastward like the Middle bar muddy facies (F4b). On the Richard tidal bar, the thickness of the groups of facies varies laterally. At the base of the bar, facies (F2) and (F3) thicken westward, while at the top of the bar facies (F4b) and (F5b) thicken eastward, suggesting that the bar was laterally accreting to the West during the deposition of facies (F2) and (F3), and to the East during the deposition of facies (F4b) and (F5b). The tidal bar is composed of sandy units (facies F2, F3 and F5a) that are vertically and laterally connected to each other (Fig. 5) and could be considered as one reservoir cell. The main reservoir heterogeneity of the Richard tidal bar is a decimetre-thick layer of Middle bar muddy facies (F4b) that completely isolates the lower part of the bar (facies F1b, F2, F3) from the upper part of the bar (facies F5b). Therefore, if the Middle bar muddy facies (F4b) is spatially continuous, the Richard tidal bar would be composed of two reservoir cells.

Six $^{14}C$ datings sampled on the three cores (Ri-2016-W, Ri-2016-C, Ri-2016-E) show very heterogeneous ages, ranging from 1996 years BP to the present. Here again, in spite of the age uncertainties, the $^{14}C$ ages indicate that the bar was deposited very recently: all but one of the $^{14}$C ages are younger than 300 years BP. The oldest age (1 996 ±25 years BP) is located in the Fluid mud facies (Fig. 6).

### 4.3. Detrital clay grain coat characterization

Clay coats correspond to a three-dimensional, clay-dominated coat around sand grains, which partially or totally covers the surface of sand grains (Dowey et al., 2017). On both tidal bars, clay coats can be observed on various framework grains (quartz, micas, feldspars, lithics), in each facies composing the tidal bars, down to a depth of almost 7 m below the surface of the bar (Figs 7 to 10). Main components are clay minerals, associated with other elements such as pyrite, diatoms, coccoliths or silt-sized quartz (Figs 7A-I and 8A-I). Diatom frustules can be observed down to the base of the cores (Figs 7F, 7I, 8E and 8I). Carbonated components (e.g. coccoliths) are more abundant in the Richard tidal bar in the outer estuary funnel (Fig. 8A and 8B). In this tidal bar, coats are also observed around bioclasts (e.g. holoturian spicules; Fig. 8A and 8B). Within both tidal bars, framboidal pyrite can be observed embedded within detrital clay grain coats (Figs 7C-D and 8C and 8D). Pyrite seems more abundant in the Richard tidal bar clay coats than in the Plassac tidal bar, but remains marginal compared to other components (average of 0.5% and 0.2% of total sample volume at Richard and Plassac, respectively).

As observed in the intertidal zone, detrital clay grain coats display various textures (Virolle et al., 2019). The commonest coat textures at Plassac are: 1) partial clay drapes, partly covering the surface of detrital grains, 2) aggregated detrital clay grain coats, scattered on the surface of sand grains and 3) bridged detrital clay grain coats, connecting detrital grains together

(Fig. 7 A-G). Aggregated clay coats are the commonest textures within the Richard tidal bar (Fig. 8A-G).

Within the Plassac tidal bar, detrital sand grains account for 59% of the total sample volume on average, and among this percentage, 22% of sand grains are coated (Table 2 and appendix S2). The abundance and distribution of coated grains associated with coat coverage classes are presented in Figure 9. On average, 6% of grains are coated by clays covering 15–30% of the grain surface (Fig. 9, Table 2). For each core from the Plassac tidal bar, detrital clay grain coats can be observed from the top to the base, down to a depth of 6.65 m (depth of the last sample in the deepest core, the PLA-2015-C; Fig. 9). For all the facies and cores gathered on the Plassac tidal bar, coated grain content is not correlated with depth, mean grain size or porosity variations.

Figure 10 shows the coated grain content evolution with associated coat coverage classes within the Richard tidal bar. Detrital clay grain coats can be observed from the top to the bottom of cores, down to a depth of 6.40 m (depth of the last sample in the deepest core, the Ri-2016-W; Fig. 10). Detrital sand grains represent on average 55% of the samples, including 13% of coated grains (Table 2). Only 3% of coated grains have a coat coverage of 15–30% of grain surfaces (Table 2). Considering all facies and cores from the Richard tidal bar, coated grain content is not correlated with depth, mean grain size or porosity variations.

Coated grain content is roughly constant along the vertical facies association of both tidal bars (Fig. 11, Table 2). For the Plassac tidal bar, the coated grain content is slightly higher in the sandiest facies (F2, F3 and F5a at 21%, 23% and 24%, respectively) and its proportion slightly decreases in muddy facies (F6 with 19%; Table 2). For the Richard tidal bar, coated grain content is comparatively steady, ranging from 11% to 17% (Table 2). Taking into account all cores, the commonest coat coverage class for both tidal bars is 5–15% (7% of coated grains for Plassac, 5% for Richard; Table 2).

### 4.4. Clay fraction and clay assemblages

For each tidal bar, the clay assemblage is composed of four clay minerals determined by XRD analysis (Fig. 12A-B): (i) chlorite, characterized by a (001) diffraction peak at 14.10 Å, (002) at 7.05 Å, (003) at 4.73 Å and (004) at 3.54 Å; (ii) illite diffraction patterns show a (001) diffraction peak around 9.99 Å, (002) at 4.99 Å and (003) at 3.33 Å; (iii) kaolinite displays a (001) diffraction peak at 7.16 Å, and a (002) diffraction peak at 3.57 Å; and (iv) smectite is identifiable after ethylene-glycol saturation, with a (001) diffraction peak close to 17 Å.

The clay fraction content is mostly located within muddy deposits (e.g. fluid mud layers, clay drapes or mud pebbles) and sand coats within samples. All samples taken together, the clay fraction content is on average *ca.* 24 wt% within the Richard tidal bar and *ca.* 30 wt% within the Plassac tidal bar (Table 2). For the Plassac tidal bar, the clay fraction is almost constant between cores, ranging from 21 wt% in PLA-2015-C to 25 wt% in PLA-2015-W (Fig. 9). There is no correlation between the clay fraction content and the porosity or the coated grain content variations in this tidal bar. For the Richard tidal bar, clay content decreases slightly towards the middle of the bar: it is *ca.* 22 wt % on Ri-2016-W, 19 wt % on Ri-2016-E and 17 wt % on Ri-2016-C (Fig. 10). Globally, there is no correlation between clay fraction content and coated grain content or porosity variations.

The clay fraction content varies between each facies. The results are presented in Table 2 and Figs 9 and 10. Mud rich facies display the highest clay fraction content (F1b, F4a, F4b and F6 with respectively 29 wt%, 58 wt%, 37 wt% and 34 wt%). In the sandy facies, the clay fraction ranges between 14 wt% and 25 wt%. The clay fraction within F1b might be underestimated because, in order to study coats, sandy ripples were oversampled compared to muddy intervals in this facies.

Within the Plassac tidal bar, semi-quantitative analyses of XRD diffractograms show that the clay fraction is, on average, mostly composed of smectite and illite (peak surface areas of 14% and 11%, respectively) with lower proportions of chlorite and kaolinite (Fig. 12A, Table 2). Clay assemblages are similar in the different cores (Fig. 9). Semi-quantitative analysis on XRD diffractograms from the Richard tidal bar clay fraction indicate that it is composed of illite, smectite, kaolinite and chlorite, with surface areas ranging on average from 16% (illite) to 2% (chlorite) of the clay fraction (Fig. 12B, Table 2).

FTIR measurements were made along each core from Plassac, and only on core Ri-2016-W from Richard (Figs 9, 10 and 12C). All the spectra obtained are similar, showing that the clay assemblage is constant overall between vertical facies associations (Fig. 12C). But a focus on specific adsorption bands, such as the water band (1900 nm) or the bands characteristic of aluminous phases (at 2200 and 2253 nm) reveals local variations (Figs 9 and 10). For the Plassac tidal bar, the water band tends to increase near the surface, especially on core PLA-2015-C (Fig. 9). It can be correlated with an increase in the contribution from swelling clay minerals, such as smectite, upwards in this core. The bands at 2200 nm ($Al_2OH$) and 2253 nm, both mainly characterizing aluminous phases such as micas or clay minerals, do not show detectable variations with depth (Fig. 9). In the Ri-2016-W core, a slight increase in each band is observed, showing an increase in the smectite contribution and in aluminous phases with depth (Fig. 10).

TEM analyses were made on isolated particles from suspended material and plotted in a ternary diagram in the $M^+$-4Si-$R^{2+}$ system (Fig. 12D). The two plotted samples (6O and 22D, respectively at 275 cm and 650 cm from the top of core PLA-2015-C) are representative of the other samples and are consistent with XRD and FTIR results. This confirms that most clay minerals belong to the families of smectite, illite and kaolinite, and that most of the particles have intermediate compositions such as those obtained through weathering processes confirming their detrital origin (Fig. 12D). Smectite is probably in a dioctahedral form, similar to montmorillonite (Fig. 12D).

# 5. Discussion

## 5.1. Relation between vertical facies associations, tidal bar internal architecture and hydrodynamic conditions

### 5.1.1. Turbidity and tidal current velocity control on tidal bar vertical facies associations

Vertical facies associations (Figs 3 and 4) observed within both tidal bars result from specific hydrodynamic processes. A coarsening-upward pattern is observed in the lower two-thirds of the bars, which is due to a thickening-upward trend of sand bed thicknesses, from the lower subtidal zone at the base of the bar (facies F1: Fluid mud facies, facies F2: Lower sand bar facies), to the upper subtidal zone (facies F3: Middle sand bar facies). They are also characterized by a fining-upward pattern, identified in the upper third of the bar, due to a thinning-upward trend of sand bed thicknesses. It is observed from the base of intertidal zone (facies F5: Upper sand bar facies) to the top of the intertidal zone (facies F6 and F7: Tidal flat and Tidal marsh facies).

Two hydrodynamic processes may explain these coarsening- and fining-upward patterns. The coarsening-upward pattern, described in the subtidal part of the tidal bars may be explained by the presence of a metre-thick fluid mud layer located at the bottom of the estuary funnel, at the base of the tidal bars.

The Fluid mud facies (F1, Figs 3 and 4) is deposited at the base of tidal bars within the FMZ that seasonally migrates with fluvial discharges variations (Fig. 13A-B). This FMZ is characterized by a very high SPM concentration (100–300 g.l$^{-1}$) and a high viscosity, which slows the tidal current velocity to below the dune migration threshold. The tidal current velocity exceeds the ripple migration threshold only.

The Lower sand bar facies (F2, Figs 3 and 4) is deposited above the FMZ, within less turbid and less viscous waters (Fig. 13 A). Consequently, the current velocity increases above the dune migration threshold and the bed thickness increases up to that of small dunes.

The Middle sand bar facies (F3, Figs 3 and 4) is deposited in major part of the subtidal zone, up to the low tide limit, in waters with a low SPM concentration (1-3 g.l$^{-1}$). The decreasing turbidity and viscosity of the water column allows an increase in the tidal current velocity and the bed thickness increases up to that of medium-size dunes.

The fining-upward pattern, observed from the base to the top of the intertidal zone, from facies F5: Upper sand bar facies, to facies F6 and F7: Tidal flat facies and Tidal marsh facies, may be explained by a tidal current velocity model presented in Fig. 13 C. It shows that in the intertidal shallow waters, the velocity of the tidal flows is reduced because the friction coefficient increases due to the reduction in the water column depth. This explains why the dunes are smaller in the Upper sand bar facies (F5) than in the subtidal Middle sand bar facies (F3), and why the current velocity falls below the dune migration threshold in the Tidal flat facies (F6) and below the ripple migration threshold in Tidal marsh facies (F7).

### 5.1.2. Short term climatic cycles control on tidal bar internal architecture

In the Gironde estuary, the extensive bathymetric map dataset compiled by the Bordeaux Harbour Authorities (Grand Port Maritime de Bordeaux) since the beginning of the twentieth century enabled the reconstruction of the morphological evolution of the inner estuary tidal bars: Trompeloup (Féniès and Tastet, 1998) and Plassac (Billy et al., 2012; Chaumillon et al. 2013). Our study presents the morphological evolution and the internal architecture of an outer estuary tidal bar (Richard). New $^{14}$C ages from the cores of Plassac and Richard tidal bars also allow us to better time-constrain their internal architecture. Based on the papers publish on the Gironde estuary (Allen, 1991; Allen and Posamentier, 1994; Féniès and Tastet, 1998; Chaumillon et al., 2013) and the use of maps of the Gironde estuary since the seventeen century (Gascuel, 2017), tidal bars are recent geobodies deposited during the last millennium.

For the Plassac tidal bar (Fig. 5), Carbon-14 ages exhibit very heterogeneous ages, ranging from 5,230 years BP to present. An age of 75 ±30 years BP at the top of the Lower sand bar facies (depth of 5.05 m) suggests that the Plassac tidal sand bar is relatively young, and was probably deposited during the last century. Older $^{14}$C ages suggest that old organic clasts could have been remobilized during recent episodes of accretion and erosion of the tidal bar. This age frame is consistent with the data published by Chaumillon et al. (2013) who demonstrate, based on the study of ancient bathymetric maps (Bordeaux Harbour Authorities), that most of the eastern spit of the Plassac tidal bar was deposited after 1908.

Billy et al. (2012) and Chaumillon et al. (2013) also demonstrate that the morphological evolution and internal architecture of the Plassac tidal bar are controlled by short term climatic cycles (Fig. 14A). During periods of high river discharge, the bar is laterally accreting and lateral accretion sand packages (LASP; named facies F1, F2, F3, F5a, in this study) are deposited. During periods of low river discharge, the lateral accretion process stops and a mud layer (named facies F4a, in this study) caps the previously deposited lateral accretion sand package.

On the Richard tidal bar (Fig. 6), in spite of age uncertainties, the $^{14}C$ datings indicate that the bar has been deposited during the modern age: all but one of the $^{14}C$ ages are younger than 300 years BP. An age of 102 ±20 years BP in the Middle sand bar facies indicates that the Richard tidal sand bar is relatively young, and was probably deposited during the last century. Here again, older $^{14}C$ ages suggest that old organic clasts could have been remobilized. The historic bathymetric maps of the Bordeaux Harbour authorities show that the Richard tidal bar was mapped for the first time in 1901, which is consistent with our radiocarbon ages. The cores sampled in the Richard tidal bar, associated with the ancient bathymetric maps allow us to reconstruct its morphological evolution over time and to understand its internal architecture (Figs 6 and 14B). The bar is composed of two vertically stacked sand bodies, separated by a muddy layer.

According to the historical charts, the lower sand body (facies F1b, F2, F3) was deposited during the first half of the twentieth century, probably between 1900 and 1940. During this period, the bar was laterally accreting landward and its volume and length increased (from 3 to 6 km long). Figure 6 shows a westward thickening of the lower sand body due to the landward migration of the bar. This period was characterized by relatively high river discharges (Fig. 15). Between 1940 and 1968, a decrease in the bar volume and length (from

6 to 2.5 km) is observed, correlated with the deposition of the muddy layer (facies F4b) at the top of the lower sand body (the $^{14}$C datings indicate put this muddy layer at 71 ±20 year BP, i.e. around 1950 ±20 - Fig. 6). At the beginning of this period, a decade of low river discharges was observed from 1942 to 1950 (Fig. 15). This low-river discharge period, associated with a lower sand supply, may have allowed the deposition of the muddy-layer (F4b). The lower sand body was probably abandoned and partially eroded before the deposition of the muddy layer. The upper sand body (facies F5b) was deposited between 1968 and probably nowadays and covered the muddy layer (facies F4b). During this period, the bar was laterally accreting seaward (Fig.14B) and its volume and length increased (from 2.5 to 7 km long). Figure 6 shows an eastward thickening of the upper sand body due to the seaward migration of the bar. This period is again characterized by relatively high river discharges (Fig. 15).

The internal architecture of the Richard tidal bar is very similar to that of the Trompeloup tidal bar, which is also made of two vertically stacked sand bodies, partially isolated from one another by a muddy layer (Féniès and Tastet, 1998).

## 5.2. Facies comparison of inner and outer tidal bars within the Gironde estuary

The Plassac tidal bar is located in the bay-head delta within the inner Gironde estuary 65 km inland from the estuary mouth, whereas the Richard tidal bar is located in the outer Gironde estuary, 25 km inland from the estuary mouth. In spite of their different locations within the estuary, the two tidal bars exhibit similar facies associations (Figs 5 and 6, Table 1). The Fluid mud facies (F1a and F1b) deposited at the base of the tidal bars shows only slight differences. Fluid mud facies F1a observed at the base of the Plassac tidal bar is composed of numerous clay drapes stacked one upon the other with interbedded silt lenses and sand ripples. It is interpreted to be a high-energy fluid mud facies (Fig. 3). Similar observations were made within the Tilje Formation with fluid mud facies in tidal-fluvial channel deposits. Ichaso and Dalrymple (2009) showed that current-generated sedimentary structures produced by the migration ripples are present. Fluid mud facies F1b observed at the base of the Richard tidal bar looks visually more homogeneous than the F1a facies, but X-rays of the facies F1b allows to see that it is stratified. It consists of numerous clay drapes stacked one upon the other alternating with very thin silt lenses. The depositional processes of facies F1a and F1b are the same, and facies F1b is interpreted to be a low-energy fluid mud facies. This facies difference might be due to the fact that the Richard tidal bar is located in the outer estuary where the high salinity gradient allows more effective flocculation of the clay minerals and consequently more mud deposition on the estuary funnel floor.

The coarsening-upward facies pattern, observed in the subtidal parts of both tidal bars, is also very similar. It is generated by a thickening-upward trend of the sandy sedimentary structures: from ripples (facies F1a,b), to small dunes (facies F2), and to large dunes (facies F3). Nevertheless a few differences can be observed in Lower sand bar facies (F2) and the Middle sand bar facies (F3): clay drapes are more abundant in the Plassac tidal bar. Their preservation is a function of the velocity of tidal currents: in the outer estuary, on the Richard bar, stronger currents erode more clay drapes.

The fining-upward pattern is better observed in the Plassac tidal bar than in the Richard tidal bar (Figs 5 and 6). It is generated by a thinning-upward trend of the sandy sedimentary structures. On the inner estuary tidal bars (Plassac and also Trompeloup, see: Féniès and Tastet, 1998), the fining-upward pattern is generated by a decrease in the size of sedimentary structures, from medium-size dunes (F3), to small dunes (F5 a,b), to the ripples and linsens (F6), and then to clay drapes (F7). On the outer estuary tidal bars (Richard), the Tidal flat facies (F6) and the Tidal marsh facies (F7) are not deposited; the fining-upward pattern is therefore generated only by the decrease in the dune size from medium-sized dunes (F3), to small dunes (F5a,b).

Quartz, feldspars and lithic grains predominate in the two bars, with sand composition ranging from litharenite to feldspathic litharenite (Fig. 2). Nevertheless, grain composition slightly differs from the two bars. The proportion of bioclastic grains is on average higher in the Richard tidal bar (6 %) compared to Plassac tidal bars (3%) with the presence of various benthic and planktonic organisms (echinoderms, foraminiferas, bivalves, Fig. 8 A-B) due to the proximity of marine sediment source. The higher salinity (18‰; Gibbs et al., 1989) in the area of the Richard tidal bar is not enough to explain a living environment for these organisms. This argues a more open marine environment for the source of these grains, probably from the tidal inlet. Clay assemblages are also slightly different: they are smectite and illite-rich for the Plassac tidal bar, and illite-rich for the Richard tidal bar (Virolle et al., 2019). Mean grain size is lower in the outer estuary (average of 153 µm for the Richard tidal bar) than in the inner estuary tidal bar (average of 225 µm for the Plassac tidal bar; Table 2). The Richard tidal bar is located within the muddy basin between two sand rich domains: the tidal inlet and the bay-head delta. At the beginning of the 20th century, the landward migration of the bar (Fig. 14B) associated with bioclastic component in cores tend to demonstrate an association with the tidal inlet dynamics. On the other hand, from 1950 to present day, the seaward migration suggests an affinity with the bay-head delta dynamic. Therefore, the Richard tidal bar seems to be a composite bar responding alternately to the dynamics of the tidal inlet and the bay-head delta and belonging to the muddy basin within the outer estuary funnel.

## 5.3. Distribution and evolution of clay minerals and detrital clay grain coats within the tidal bars

### 5.3.1. Clay mineral distribution in relation to hydrodynamic conditions

TEM analyses show that the clay particles forming clay coats have intermediate compositions like those obtained through weathering processes (Fig. 12D). Therefore, we postulate that these particles are detrital, and not neo-formed or authigenic. The coats are mainly composed of dioctahedral smectite and illite with lower amounts of kaolinite (Fig. 12D).

The local increase in the water band in FTIR, as observed near the surface of the PLA-2015-C core or more deeply in the Ri-2016-W core, may be associated with an increased contribution from swelling minerals such as smectite (Figs 9 and 10). FTIR measurements using a portable spectrometer allow detecting rapidly aluminous phases such as micas or clay minerals in sands. Specific bands such as the water band at 1900 nm or the bands at 2200 nm and 2253 nm, characteristic of aluminous phases, reveals local variations of clay minerals as smectite for example. Local hydrodynamic conditions along the estuary can explain this distribution (Gibbs, 1983; Chamley, 1989; McAnally and Mehta, 2000; Whitehouse, 2000; Worden and Morad, 2003). The Gironde estuary TMZ is rich in smectite and illite, which is deposited through biologically or chemically-induced flocculation (Latouche et al., 1991; Gibbs, 1983). Recent studies have shown that the decline in flood periods in the estuarine system, and the longer duration of low-river stages, maintains the TMZ in the upstream part of the estuary from the inner part of the inner estuary funnel to the estuarine channels (Jalon-Rojas et al., 2015). This could explain why more smectite is deposited and preserved in the intertidal zone of the Plassac tidal bar. It may also account for the higher clay fraction content in the Plassac tidal bar than the Richard tidal bar (Table 2).

### 5.3.2. Detrital clay grain coat composition, origin and distribution within modern estuarine tidal bars

Detrital clay grain coat textures such as the ridged, aggregated or bridged textures observed in cores sampled along the inner and outer tidal bars (Plassac and Richard) are consistent with those reported in the intertidal zone of tidal bars of the Gironde and the Ravenglass estuaries (Virolle et al., 2019, Wooldridge et al., 2017, 2019). In the Gironde estuary, the clay mineral assemblage is relatively similar in the cores and at the surface of tidal bars (illite, smectite, chlorite and kaolinite), pointing to a relative stability in the composition of clay assemblages in the TMZ during the last centuries. The clay assemblage differs in other modern estuaries such as the Ravenglass estuary whose clay assemblage is marked by the absence of smectite and where clay mineral distribution is controlled by estuarine hydrodynamics (Wooldridge et al., 2018, Griffiths et al., 2018, 2019b). However, within both the Gironde and the Ravenglass estuaries, post-depositional processes, as early-diagenetic mineral alteration through continued weathering of silicate minerals, do not influence clay-mineral distribution patterns in near-surface sediment (Griffiths et al., 2019a and 2019b).

In the Gironde, coats contain other components including silt-sized quartz, carbonates and pyrite embedded within detrital clay grain coats (Figs 7 C-D and 8 C-D). Pyrite has also been observed in short cores (1 m) from the Ravenglass estuary, mainly in mud flats and mixed flats in the center basin (Griffiths et al., 2018). The formation of sedimentary iron sulphides via bacterial sulphate reduction in marine systems is well known (Berner, 1967, 1970). Even in marginal proportions (less than 1% of the total volume), it shows that iron is present in the water column of the estuary (Robert et al., 2004; Audry et al., 2007). As within the Ravenglass, carbonates abundance decrease with increasing grain size when moving toward the inner estuary (Griffiths et al., 2019b).

The Plassac tidal bar has, on average, more coated grain content (22% of detrital grains) than the Richard tidal bar (13%; Table 2), as is the case within surface sediments (Virolle et al., 2019).

Clay content and coated grain content within the Gironde estuary tidal bar deposits could be mostly related to hydrodynamic variations (as the seasonal TMZ position changes). There is no evidence of mechanical infiltration and very scarce bioturbation in the studied cores. If these post-depositional processes have occurred, they have not significantly influenced the distribution of detrital clay grain coats in surface sediment or in the vertical facies associations of the tidal bars.

In the intertidal zone of the Gironde estuary tidal bars and point bars, detrital clay grain coats are mostly formed through the interaction of clay minerals and exopolymeric substances (EPSs) mostly produced by diatoms (Virolle et al., 2019). EPSs may act as a glue allowing clay particles to adhere to detrital grains (Jones et al., 2017; Wooldridge et al., 2017, Virolle et al., 2019). Both optical microscopy and SEM observations confirm that diatoms are present inside clay coats in both tidal bars down to several metres below the surface (Fig. 7F, 7I and 8E). Additional studies will have to be carried out to determine whether EPSs are preserved during burial and play a part in the preservation of clay coats within tidal bars.

### 5.4. Reservoir potential of inner and outer estuary tidal bars

The reservoir potential of the Plassac and Richard tidal bars is studied at different scales (i) macroscopic scale (dimensions and internal architecture of the bars), (ii) mesoscopic scale (facies composition), and (iii) microscopic scale (coated grain content and clay fraction).

On the macroscopic scale, the Plassac tidal bar is 4.6 km long, 1.4 km wide and the maximum sand thickness reaches 5.60 m (core PLA-2015-C, Fig. 16). The Richard tidal bar is smaller: 4 km long, 300 m wide and the maximum sand thickness reaches 3.50 m (core Ri-2016-W). The Gironde estuary bar size is comparable to the size of many ancient estuarine tidal bars, e.g., in the Permian Cape Hay Formation (Australia; Saïag et al., 2016), in the Early Jurassic Tilje Formation (Norway; Nordahl et al., 2006; Martinius et al., 2011) and in the Early Cretaceous Sego Formation (United States; Aschoff et al., 2016).

Both tidal bars are composed of stacked sand bodies, separated by muddy internal seals, which may partition the bars into different reservoir cells (Figs 5 and 6). These sand bodies may be laterally juxtaposed (Plassac tidal bar), or vertically stacked (Richard tidal bar) due to very different processes. The Plassac tidal bar is composed of two lateral accretion sand packages (facies: F2, F3 and F5a), separated by a decimetre-thick muddy layer (facies F4a), which dips gently eastward (3° dip-angle) in a direction normal to the axis of the tidal currents. Its internal architecture records the lateral migration of a single tidal bar, punctuated by phases of growth and abandonment. The Richard tidal bar is a composite geobody, made of two stacked sandy tidal bars, separated by a decimetre-thick muddy layer (Fig. 6). The lower sand body (facies F2, F3) was deposited during the lateral migration of a first tidal bar. It was then abandoned, partially eroded and capped by a muddy layer (facies F4b), dipping gently eastward (1.5° dip-angle). Finally, the upper sand body (facies F5b) was deposited during the lateral migration of a second tidal bar, on top of the muddy layer (facies F4b). The internal architecture of the Richard tidal bar is very similar to that of the Trompeloup tidal bar which is also composed of two stacked individual tidal bars, separated by a thick muddy layer (Féniès and Tastet, 1998).

On the mesoscopic scale, the reservoir facies of the Plassac and Richard tidal bars (facies F2, F3, F5a, F5b, Fig. 16) are mostly composed of sand dunes exhibiting variable clay drape content. Those millimetre-thick clay drapes are a few metres long and wide. In terms of reservoir capacity, those clay drapes will reduce the vertical permeabilities and could act as potential fluid and pressure baffles. The Middle bar facies (F3) could be considered as the best reservoir facies on the mesoscopic scale due to the low abundance of preserved clay drapes; the Lower sand bar facies (F2) might be the poorest quality reservoir facies due to the numerous clay drapes preserved. The Upper sand bar facies (F5) shows a noticeable difference between the inner and outer estuary tidal bars: in the Plassac tidal bar the (F5a) facies contains abundant clay drapes and mud pebbles, whereas in the Richard tidal bar, the (F5b) facies is characterized by the absence of clay drapes that would acted as baffles and therefore could be considered a better reservoir (Fig. 16).

On the microscopic scale, the distribution of detrital clay grain coats is a major parameter controlling quartz cement inhibition and the preservation of porous space if the sand bars are deeply buried (Fig. 16). On the contrary, the total volume of clays will probably result in authigenic clay minerals blocking pore throats and drastically reducing permeability at great burial depths (Worden and Morad, 2003; Wooldridge et al., 2017; Griffiths et al., 2018). Those parameters are analysed in detail for each tidal bar facies (Table 2). The Middle bar facies (F3) could be considered as the best reservoir facies of both tidal bars if deeply buried, because it contains the minimum clay fraction (15 wt% and 14 wt% for Plassac and Richard respectively), while exhibiting a fairly high coated grain content (R=12%, P=23%). The Richard tidal bar has higher porosities values (*ca*. 34%) than the Plassac tidal bar (*ca*. 25%). The Plassac tidal bar has a higher proportion of coated grains than the Richard tidal bar (av.: 22% vs. 13%) and the total volume of the clay fraction is higher at Plassac than at Richard (av.: 30 wt% vs. av.: 24 wt%). At Plassac, 6% of grains are coated by clay which covers 15–30% of the grain surface. At Richard, only 3% of grains are coated by clay, covering 15–30% of the grain surface (Table 2). Consequently, on the microscopic scale, the Richard tidal bar will provide the best reservoir potential if deeply buried, with about 15% of coated grain and about 25% of total volume of clays. Besides, porosity can be enhanced through carbonates dissolution as it can occur in Richard tidal bar, richer in carbonates. Remaining porosity during subsequent compaction may be preserved through early carbonate cement formation that can increase the mechanical strength of sediments (Morris et al., 2006). Therefore, as it can be observed in the Ravenglass estuary, better reservoir quality may be found in estuarine depositional environments that initially contained a small amount of carbonate material (Griffiths et al., 2019). Outer estuarine tidal bars might therefore the best prospects for reservoirs qualities at great depth. The Plassac tidal bar may experience more intense matrix formation during eodiagenesis owing to plastic deformation and compaction of ductile grains (clay drapes and mud pebbles) between rigid grains (Morad et al., 2010). Higher coated grain content can also obstruct porosity throats during compaction affecting reservoir qualities.

## 6. Conclusion

This multi-scale study aims to better understand processes governing the facies associations, reservoir architecture, and distribution of detrital clay grain coats and clay minerals within two tidal bars deposited in the Gironde estuary: the Plassac tidal bar in the inner estuary funnel and the Richard tidal bar in the outer estuary funnel. Although these tidal bars are 40 km apart, they are characterized by similar vertical facies associations which result from specific hydrodynamic processes that are generated in very turbid estuaries.

On a larger scale, the overall dimensions of both tidal bars are comparable to those observed in ancient estuaries. They are 4 to 5 km long, 300 to 1400 m wide and their maximum individual sand thickness ranges from 3.5 to 5.6 m.

Their internal architecture shows that the two tidal bars are composite geobodies made of stacked sand units, separated by muddy internal seals partitioning the bars into different reservoir cells. For both bars, the alternating periods of sand deposition (Lateral Accretion Sand Packages or individual tidal bars) and mud deposition (muddy internal seals) may be controlled by short term (multi-annual) climatic cycles.

On a smaller scale, detrital clay grain coats are observed from the top to the base of both tidal bars, in the entire intertidal and subtidal zones. Coats are mainly composed of clay minerals (dioctahedral smectite, illite, kaolinite and chlorite), associated with a minor proportion of other elements such as silt-sized quartz, coccoliths, pyrite or diatoms frustules. Clay minerals can be rapidly detected using a portable spectrometer. Globally, clay assemblage is the same from the top to the bottom of tidal bars. Variations of specific bands as the ones at 1900 nm, 2200 nm or 2253 nm reveal local variations of some clay minerals as smectite. The clay fraction and coated grain content are higher in the inner estuary Plassac tidal bar than in the outer estuary Richard tidal bar probably due to the more regular presence of TMZ in the Plassac area. Tidal bars deposited in the outer estuary present the optimum coated grain content (about 15% of grains are coated), coat coverage (extent of grain covered by clays reach about 5–15%) and clay fraction volume (about 25%). Outer estuary tidal bars are more likely to offer the best reservoir quality in terms of porosity and permeability after burial. This study has shown that multi-scale processes can influence reservoirs quality distribution and prediction at great depth. Results may be used to better predict and understand sandstone reservoir quality in similar estuarine sandstones reservoirs.

## ACKNOWLEDGMENTS

This work is the result of collaborative project No P04980 CLAYCOAT “CLAY COATing in shallow marine clastic deposits to improve reservoir quality prediction” between University Paris-Sud, Bordeaux INP, University of Bordeaux Montaigne, University of Poitiers and ENGIE (Neptune Energy since 2018). This study has benefitted greatly from ENGIE and Neptune Energy funding. The authors would also like to thank the Bordeaux Harbour Authorities for providing bathymetric data of the Gironde estuary. We thank Julius Nouet (GEOPS) for assistance with SEM observations. We are grateful to Léa Pigot (ENSEGID), Valérie Godard (GEOPS) and Philippe Blanc (Lithologie Bourgogne) for high-quality thin sections. We also wish to thank the “Sediment Archive Analysis” Platform at the EPOC laboratory (Bordeaux, France), and especially Isabelle Billy, Pascal Lebleu and Olivier Ther for their support during the core description. We thank Marc Massault for assistance during graphite preparation and during $^{14}$C counting performed at Gif-sur-Yvette using AMS ECHoMICADAS. And finally, we thank N'Guessan Essey and Aude Cumont from the University of Poitiers, Flora Guillemaut and Violaine Gascuel from the ENSEGID (Bordeaux INP) for their contributions to this study. We also thank the associate editor, Andrew Green, Bernadette Tessier and an anonymous reviewer who provided insightful and helpful comments that improved the final manuscript.

## References

Aase, N.E., Bjorkum, P.A., Nadeau, P.H., 1996. The Effect of Grain-Coating Microquartz on Preservation of Reservoir Porosity. AAPG Bulletin 80 (10), 1654–1673.

Allen, G.P., 1972. Etude des processus sédimentaires dans l'estuaire de la Gironde. Thèse Doctorat des Sciences, Université de Bordeaux I, No. 353, 314 pp.

Allen, G.P., Bonnefille, R., Courtois, G., Migniot, C., 1974. Processus de sédimentation des vases dans l'estuaire de la Gironde Contribution d'un traceur radioactif pour l'étude du déplacement des vases. La Houille Blanche 1-2, 129-136.

Allen, G.P., Sauzay, G., Castaing, P., Jouanneau, J.M., 1977. Transport and deposition of suspended sediment in the Gironde Estuary, France. Estuarine Processes 2, 63-81.

Allen, G.P., 1991. Sedimentary processes and facies in the Gironde estuary: a recent model for macrotidal estuarine systems. In: Clastic Tidal Sedimentology (Eds R.A. Rahmani, D.G. Smith, G.E. Reinson and B.A. Zaitlan), Memoir 16, 29-39.

Allen, G.P., Posamentier, H.W., 1994. Transgressive facies and sequence architecture in mixed tide-and wave-dominated incised valleys: example from the Gironde Estuary, France. In: Incised-valley Systems: Origins and Sedimentary Sequences (Eds R.W. Dalrymple, R. Boyd and B.A. Zaitlin), SEPM Special Publication 51, 225-240.

Allen, G.P., Salomon, J.C., Bassoullet, P., Du Penhoat, Y., De Grandpre, C., 1980. Effects of tides on mixing and suspended sediment transport in macrotidal estuaries. Sedimentary Geology 26, 69–90.

Aschoff, J.L., Olariu, C., Steel, R.J., 2018. Recognition and significance of bayhead delta deposits in the rock record: A comparison of modern and ancient systems. Sedimentology 65, 62–95.

Audry, S., Blanc, G., Schäfer, J., Robert, S., 2007. Effect of estuarine sediment resuspension on early diagenesis, sulfide oxidation and dissolved molybdenum and uranium distribution in the Gironde estuary, France. Chemical Geology 238, 149-167.

Berner, R., 1967. Thermodynamic stability of sedimentary iron sulfides. American Journal of Science 265, 773-785.

Berner, R., 1970. Sedimentary pyrite formation. American Journal of Science 268, 1–23.

Beaufort, D., Rigault, C., Billon, S., Billault, V., Inoue, A., Inoue, S., Patrier, P., 2015. Chlorite and chloritization processes through mixed-layer mineral series in low-temperature geological systems-a review. Clay Minerals 50, 497-523.

Billy, J., Chaumillon, E., Féniès, H., Poirier, C., 2012 Tidal and fluvial controls on the morphological evolution of a lobate estuarine tidal bar: The Plassac Tidal Bar in the Gironde Estuary (France). Geomorphology 169–170, 86–97.

Bjørlykke, K., 2014. Relationships between depositional environments, burial history and rock properties. Some principal aspects of diagenetic process in sedimentary basins. Sedimentary Geology 301, 1–14.

Bjorlykke, K., Egeberg, P.K., 1993. Quartz cementation in sedimentary basins. AAPG Bulletin 77, 1538–1548.

Bloch, S., Lander, R.H., Bonnell, L., 2002. Anomalously high porosity and permeability in deeply buried sandstone reservoirs: Origin and predictability. AAPG Bulletin 86, 303-328.

Bonneton, P., Bonneton, N., Parisot, J.-P., Castelle, B., 2015. Tidal bore dynamics in funnel-shaped estuaries. Journal of Geophysical Research: Oceans 120, 923–941.

Castaing, P., 1981. Le transfert à l'océan des suspensions estuariennes : cas de la Gironde. Mémoires de l'Institut De Géologie Du Bassin D'Aquitaine 12, 530 p.

Chamley, H., 1989. Clay Sedimentology. Springer Berlin Heidelberg, Berlin, Heidelberg.

Chanson, H., Reungoat, D., Simon, B., Lubin, P., 2011. High-frequency turbulence and suspended sediment concentration measurements in the Garonne River tidal bore. Estuarine and Coastal Shelf Science 95, 298-306.

Chaumillon, E., Féniès, H., Billy, J., Breilh, J.-F., Richetti, H., 2013. Tidal and fluvial controls on the internal architecture and sedimentary facies of a lobate estuarine tidal bar (The Plassac Tidal Bar in the Gironde Estuary, France). Marine Geology 346, 58–72.

Dalrymple, R.W., Zaitlin, B.A., Boyd, R., 1991. Estuarine facies models: Conceptual basis and stratigraphic implications. Journal of Sedimentary Research 62, 1130–1146.

Deschamps, R., Guy, N., Preux, C., Lerat, O., 2012. Analysis of Heavy Oil Recovery by Thermal EOR in a Meander Belt: From Geological to Reservoir Modeling. Oil Gas Sci. Technol. – Revue D'IFP Energies Nouvelles 67, 999–1018.

Doxaran, D., Froidefond, J.-M., Castaing, P., Babin, M., 2009. Dynamics of the turbidity maximum zone in a macrotidal estuary (the Gironde, France): Observations from field and MODIS satellite data. Estuarine, Coastal and Shelf Science 81, 321–332.

Ehrenberg, S.N., 1989. Assessing the Relative Importance of Compaction Processes and Cementation to Reduction of Porosity in Sandstones: Discussion; Compaction and Porosity Evolution of Pliocene Sandstones, Ventura Basin, California: Discussion. AAPG Bulletin 73, 1274-1276.

Ehrenberg, S.N., 1993. Preservation of anomalously high porosity in deeply buried sandstones by grain coating chlorite: examples from the Norwegian continental shelf. AAPG Bulletin 77, 1260–1286.

Etcheber, H., Jouanneau, J.M., Latouche, C., Azoeuf, P., Caillot, A., Hoslin, R., 1980. L'expérience "double marquage de vase en Gironde". Contribution à la connaissance du devenir d'une pollution métallique en estuaire. Oceanologica acta 3, 477-486.

Etcheber, H., Schmidt, S., Sottolichio, A., Maneux, A., Chabaux, G., Escalier, J.M, Wennekes, H., Derrienic, H., Schmeltz, M., Quéméner, L., Repecaud, M., Woerther, P., Castaing, P., 2011. Monitoring water quality in estuarine environments: lessons from the MAGEST monitoring program in the Gironde fluvial-estuarine system. Hydrology and Earth System Sciences 15, 831-840.

Féniès, H., Resseguier, A.D., Tastet, J.-P., 1999. Intertidal clay-drape couplets (Gironde estuary, France). Sedimentology 46, 1–15.

Féniès, H., Tastet, J.-P., 1998. Facies and architecture of an estuarine tidal bar (the Trompeloup bar, Gironde Estuary, SW France). Marine Geology 150, 149–169.

Féniès, H., Lericolais, G., Posamentier, H.W., 2010. Comparison of wave- and tide-dominated incised valleys: specific processes controlling systems tract architecture and reservoir geometry. Bulletin of the French Geological Society 181, 171-181

Gascuel, V., 2017. Analyse de l'évolution morphologique de barres de marées de l'estuaire de la Gironde : Etude del'évolution des barres de Bordeaux, Plassac, Trompeloup, et Richard en relation avec les processus sédimentaires et anthropiques. Mem. Stage 2eme année en école d'ingénieur, ENSEGID, Bordeaux INP.

Gibbs, R.J., 1983. Coagulation rates of clay minerals and natural sediments. Journal of Sedimentary Research 53, 1193-1203.

Gibbs, R.J., Tshudy, D.M., Konwar, L. and Martin, J., 1989. Coagulation and transport of sediments in the Gironde Estuary. Sedimentology 36, 987–999.

Gascuel, V., 2017. Analyse de l'évolution morphologique de barres de marées de l'estuaire de la Gironde : Etude del'évolution des barres de Bordeaux, Plassac, Trompeloup, et Richard en relation avec les processus sédimentaires et anthropiques. Mem. Stage 2$^{eme}$ année en école d'ingénieur, ENSEGID, Bordeaux INP, 85 p.

Gibert, E., Bergonzini, L., Massault, M., Williamson, D., 2002. AMS-14C chronology of 40.0 cal ka BP continuous deposits from a crater lake (Lake Massoko, Tanzania) Modern water balance and environmental implications. Paleogeography Paleoclimatology Paleoecology 187, 307–322.

Gould, K., Pe-Piper, G., Piper, J.W., 2010. Relationship of diagenetic chlorite rims to depositional facies in Lower Cretaceous reservoir sandstones of the Scotian Basin, Sedimentology 57, 587-610.

Griffiths, J., Worden, R. H., Wooldridge, L. J., Utley, J. E., Duller, R. A., 2018. Detrital clay coats, clay minerals, and pyrite: a modern shallow-core analogue for ancient and deeply buried estuarine sandstones. Journal of Sedimentary Research, 881, 1205-1237.

Griffiths, J., Worden, R. H., Wooldridge, L. J., Utley, J. E., Duller, R. A., Edge, R. L., 2019a. Estuarine clay mineral distribution: Modern analogue for ancient sandstone reservoir quality prediction. Sedimentology 66, 2011-2047.

Griffiths, J., Worden, R. H., Wooldridge, L. J., Utley, J. E., Duller, R. A., 2019b. Compositional variation in modern estuarine sands: predicting major controls on sandstone reservoir quality. AAPG Bulletin 103, 797-833.

Grim, R.E., 1942. Modern concepts of clay materials. The Journal of Geology 50, 225–275.

Guillemaut, F., 2016. Etude faciologique et pétrographique des barres de marée (Plassac, Gironde) : Prédiction de la distribution du coating argileux. Mem. Stage 3$^{eme}$ année en école d'ingénieur, ENSEGID, Bordeaux INP, 59 p.

Jackson, M.D., Muggeridge, A.H., Yoshida, S., Johnson, H.D., 2003. Upscaling Permeability Measurements Within Complex Heterolithic Tidal Sandstones. Mathematical Geology 35, 499-520.

Jackson, M.D., Yoshida, S., Muggeridge, A.H., Johnson, H.D., 2005. Three-dimensional reservoir characterization and flow simulation of heterolithic tidal sandstones. AAPG Bulletin 89, 507–528.

Jalón-Rojas, I., Schmidt, S., Sottolichio, A., 2015. Turbidity in the fluvial Gironde Estuary (southwest France) based on 10-year continuous monitoring: sensitivity to hydrological conditions. Hydrology and Earth System Sciences 19, 2805–2819.

Jones, S., 2017. Goo, glue, and grain binding: importance of biofilms for diagenesis in sandstones. Geology 45, 959-960.

Latouche, C., Jouanneau, J.M., Lapaquellerie, Y., Maillet, N., Weber, O., 1991. Répartition des minéraux argileux sur le plateau continental Sud-Gascogne. Oceanologica Acta. Actes du Colloque International sur l'environnement des mers épicontinentales, Lille, 155-161.

Legler, B., Johnson, H.D., Hampson, G.J., Massart, B.Y.G., Jackson, C.A.-L., Jackson, M.D., El-Barkooky, A., Ravnas, R., 2013. Facies model of a fine-grained, tide-dominated delta: Lower Dir Abu Lifa Member (Eocene), Western Desert, Egypt. Sedimentology 60, 1313–1356.

Lericolais, G., Féniès, H., Tastet, J.-P., Berné, S., 1998. Reconnaissance par stratigraphie sismique haute résolution de la paléovallée de la Gironde sur le plateau continental. Comptes Rendus Académie Sci.-Ser. IIA-Earth and Planetary Science 326, 701–708.

Mallet, C., Howa, H.L., Garlan, T., Sottolichio, A., Le Hir, P., 2000. Residual Transport Model in Correlation with Sedimentary Dynamics over an Elongate Tidal Sandbar in the Gironde

Estuary (Southwestern France). Journal of Sedimentary Research 70, 1005–1016.

Martinius, A.W., Ringrose, P.S., Brostrom, C., Elfenbein, C., Naess, A., Ringas, J.E., 2005. Reservoir challenges of heterolithic tidal sandstone reservoirs in the Halten Terrace, mid-Norway. Petroleum Geoscience 11, 3–16.

Martinius, A.W., Berg, J.H., Buller, A.T., 2011. Atlas of sedimentary structures in estuarine and tidally-influenced river deposits of the Rhine-Meuse-Scheldt system: their application to the interpretation of analogous outcrop and subsurface depositional systems. EAGE Publications, Houten, 298 p.

Massart, B.Y.G., 2014. Improved characterisation and modelling of heterolithic tidal sandstone reservoirs. Imperial college London, London, 224 p.

McAnally, W.H., Mehta, A.J., 2000. Aggregation rate of fine sediment. Journal of Hydraulic Engineering 126, 883–892.

Meunier, A., Velde, B., 1989. Solid solutions in I/S mixed-layer minerals and illite. American Mineralogist 74, 1106-1112.

Morad, S., Al-Ramadan, K., Ketzer, J.M., De Ros, L.F., 2010. The impact of diagenesis on the heterogeneity of sandstone reservoirs: a review of the role of depositional facies and sequence stratigraphy. AAPG Bulletin 94, 1267-1309.

Morris, J. E., Hampson, G. J., Johnson, H. D., 2006. A sequence stratigraphic model for an intensely bioturbated shallow-marine sandstone: the Bridport Sand Formation, Wessex Basin, UK: Sedimentology 53, 1229-1263.

Musial, G., Reynaud, J.-Y., Gingras, M.K., Féniès, H., Labourdette, R., Parize, O., 2012. Subsurface and outcrop characterization of large tidally influenced point bars of the Cretaceous McMurray Formation (Alberta, Canada). Sedimentary Geology 279, 156–172.

Nordahl, K., Ringrose, P.S., Wen, R., 2005. Effective permeability of a heterolithic tidal reservoir interval using a process-orientated modelling tool. Petroleum Geoscience 11, 17–28.

Nordahl, K., Martinius, A.W., Kritski, A., 2006. Time-series analysis of a heterolithic, ripple-laminated deposit (Early Jurassic, Tilje Formation) and implications for reservoir modelling. Marine Geology 235, 255–271.

Nordahl, K., Ringrose, P.S., 2008. Identifying the Representative Elementary Volume for Permeability in Heterolithic Deposits Using Numerical Rock Models. Mathematical Geoscience 40, 753–771.

Olariu, M.I., Olariu, C., Steel, R.J., Dalrymple, R.W, Martinius, A.W., 2012. Anatomy of a laterally migrating tidal bar in front of a delta system: Esdolomada Member, Roda Formation, Tremp-Graus Basin, Spain: Esdolomada tidal bar. Sedimentology 59, 356–378.

Pe-Piper, G., Weir-Murphy, S., 2008. Early diagenesis of inner shelf phosphorite and iron-silicate minerals, Lower Cretaceous of Orpheus graben, southeastern Canada: implications for the origin of chlorite rims. AAPG Bulletin 92, 1153–1168.

Pittman, E.D., Larese, R.E., Heald, M.T., 1992. Origin, Diagenesis, and Petrophysics of Clay Minerals in Sandstones. (Eds Houseknecht, D.W., Pittman, E.D). SEPM Special Publication 47, 241-255.

Reineck, H.-E., Wunderlich, F., 1968. Classification and origin of flaser and lenticular bedding. Sedimentology 11, 99–104.

Ringrose, P., Nordahl, K., Wen, R., 2005. Vertical permeability estimation in heterolithic tidal deltaic sandstones. Petroleum Geoscience 11, 29–36.

Robert, S., Blanc, G., Schäfer, J., Lavaux, G., Abril, G., 2004. Metal mobilization in the Gironde Estuary (France): the role of the soft mud layer in the maximum turbidity zone. Marine Chemistry 87, 1-13.

Roduit, N., 2007. JMicroVision: un logiciel d'analyse d'images pétrographiques polyvalent. Section des Sciences de la Terre, Université de Genève, Genève, 129 p.

Saïag, J., Brigaud, B., Portier, É., Desaubliaux, G., Bucherie, A., Miska, S., Pagel, M., 2016. Sedimentological control on the diagenesis and reservoir quality of tidal sandstones of the Upper Cape Hay Formation (Permian, Bonaparte Basin, Australia). Marine and Petroleum Geology 77, 597–624.

Savoye, N., David, V., Morisseau, F., Etcheber, H., Abril, G., Billy, I., Charlier, K., Oggian, G., Derriennic, H., Sautour, B., 2012. Origin and composition of particulate organic matter in a macrotidal turbid estuary: The Gironde Estuary, France. Estuarine, Coastal and Shelf Science 108, 16–28.

Shchepetkina, A., Gingras, M.K., Pemberton, S.G., 2016. Sedimentology and ichnology of the fluvial reach to inner estuary of the Ogeechee River estuary, Georgia, USA. Sedimentary Geology 342, 202–217.

Shchepetkina, A., Gingras, M. K., Pemberton, S. G., 2018. Modern observations of floccule ripples: petitcodiac River estuary, New Brunswick, Canada. Sedimentology 65 , 582-596.

Sottolichio, A., Castaing, P., 1999. A Synthesis on seasonnal dynamics of highly-concentrated structures in the Gironde estuary. Compte Rendu de l'Académie des Sciences- Séries IIA- Earth and Planetary Science 329, 795–800.

Sottolichio, A., Castaing, P., Etcheber, H., Maneux, E., Schmeltz, M., Schmidt, S., 2011. Observations of suspended sediment dynamics in a highly turbid macrotidal estuary, derived from continuous monitoring. Journal of Coastal Research 64, 1579-1583.

Storvoll, V., Bjørlykke, K., Karlsen, D., Saigal, G., 2002. Porosity preservation in reservoir sandstones due to grain-coating illite: a study of the Jurassic Garn Formation from the Kristin and Lavrans fields, offshore Mid-Norway. Marine and Petroleum Geology 19, 767–781.

Stricker, S., Jones, S.J., 2018. Enhanced porosity preservation by pore fluid overpressure and chlorite grain coatings in the Triassic Skagerrak, Central Graben, North Sea, UK. Geological Society London Special Publication 435, 321–341.

Taylor, T.R., Kittridge, M.G., Winefield, P., Bryndzia, L.T., Bonnell, L.M., 2015. Reservoir quality and rock properties modeling – Triassic and Jurassic sandstones, greater Shearwater area, UK Central North Sea. Marine and Petroleum Geology 65, 1–21.

Tessier, B., Billeaud, I., Sorrel, P., Delsinne, N., Lesueur, P., 2012. Infilling stratigraphy of macrotidal tide-dominated estuaries. Controlling mechanisms: Sea-level fluctuations, bedrock morphology, sediment supply and climate changes (The examples of the Seine estuary and the Mont-Saint-Michel Bay, English Channel, NW France). Sedimentary Geology 279, 62-73.

Virolle, M., Brigaud, B., Bourillot, R., Féniès, H., Portier, E., Duteil, T., Nouet, J., Patrier, P., Beaufort, D., 2019. Detrital clay grain coats in estuarine clastic deposits: origin and spatial distribution within a modern sedimentary system, the Gironde Estuary (south-west France). Sedimentology 66, 859-894.

Visser, M. J., 1980. Neap-spring cycles reflected in Holocene subtidal large-scale bedform deposits: a preliminary note. Geology 8, 543-546.

Weber, K. J., 1986. How heterogeneity affects oil recovery. In: Reservoir Characterization. Eds Lake, L.W. and Carroll, H.B. Academic Press, New York, NY, 487-544.

Whitehouse, R., Soulsby, R., Roberts, W., Mitchener, H., 2000. Dynamics of estuarine muds: a manual for practical applications. Telford, London, 232 p.

Wood, L.J., 2004. Predicting Tidal Sand Reservoir Architecture Using Data from Modern and Ancient Depositional Systems. AAPG Memoir 80, 45–66.

Wooldridge, L.J., Worden, R.H., Griffiths, J., Utley, J.E.P., 2017a. Clay-Coated Sand Grains In Petroleum Reservoirs: Understanding Their Distribution Via A Modern Analogue. Journal of Sedimentary Research 87, 338–352.

Wooldridge, L. J., Worden, R. H., Griffiths, J., Thompson, A., Chung, P., 2017b. Biofilm origin of clay-coated sand grains. Geology 45, 875-878.

Wooldridge, L. J., Worden, R. H., Griffiths, J., Utley, J. E., 2019. How To Quantify Clay-Coat Grain Coverage in Modern and Ancient Sediments. Journal of Sedimentary Research 89, 135-146.

Worden, R.H., Morad, S., 2003. Clay minerals in sandstones: controls on formation, distribution and evolution, in: Worden, R.H., Morad, S. (Eds.), Clay mineral cements in sandstones. Special Publication of the International Association of Sedimentologists. Blackwells, Oxford, pp. 3-41.

Yoshida, S., Johnson, H.D., Gupta, R., Martinius, A.W. (Eds.), 1999. Advanced Reservoir Characterization for the 21st Century: 19th Annual. Presented at the GCSSEPM Foundation 19th Annual Research Conference Advanced Reservoir Characterization, Society of Economic Paleontologists and Mineralogists, 100–108.

## FIGURE CAPTIONS

**Figure 1:** Study area location with simplified sedimentological map of the Gironde estuary (France). Zooms of the two tidal bars are illustrated: the elongated Richard tidal bar on the left and the lobate tidal bar on the right with sedimentary environments replaced on

pictures. Bathymetric maps originate from the Atlantic Port of Bordeaux bathymetric map that cover the entire estuary. ***2 columns fitting image***

**Figure 2:** Petrographic composition of the framework sand grains from both tidal bars plotted on a QFL (Q- Quartz, F- Feldspars, L- Lithic fragment) diagram (after Folk, 1980). ***1.5 column fitting image***

**Figure 3:** Synthetic log representative of the Plassac tidal bar vertical facies successions. The log is coloured according to the alternating sandy or clayey facies. Pictures in the middle illustrate the surface equivalent and position of facies described in cores. Illustrations on the right show representative sections of described facies with their interpretation in terms of sedimentary structures. LWST = Low Water of Spring Tides. ***2 columns fitting image***

**Figure 4:** Synthetic log representative of the Richard tidal bar vertical facies successions. The log is coloured according to the facies. Pictures in the middle illustrate the surface equivalent and position of facies described in cores. Illustrations on the right show representative sections of described facies with their interpretations in terms of sedimentary structures. LWST = Low Water of Spring Tides. ***2 columns fitting image***

**Figure 5:** Plassac tidal bar cross-section showing correlation between cores and the internal architecture of the tidal bar. Carbon 14 datings are also placed alongside cores. Correlations lines are timelines, because they are coherent with the very high resolution seismic lines shot across the bar (see Chaumillon at al., 2013, Fig. 3A, line GiRaFS_65). Ages are not

considered to be a good correlation tool as the organic matter debris may have been initially deposited much before the genesis of the bar in an upstream location (e.g. estuarine channels) and then eroded, transported downstream and incorporated into the tidal bar. LWST = Low Water of Spring Tides. ***2 columns fitting image***

**Figure 6:** Richard tidal bar cross-section showing correlation between cores and the internal architecture of the tidal bar. Carbon 14 datings are also placed alongside cores. Correlations are mainly based on facies observations. LWST = Low Water of Spring Tides. ***2 columns fitting image***

**Figure 7:** Representative microphotographs under optical microscope and SEM showing grain composition and the textural characteristics of sand coats within the Plassac tidal bar. A-B) Microphotographs showing quartz (Qz), Feldspars (Fd) and lithic (Li) detrital grains and brown detrital clay minerals surrounding framework grains, forming Detrital Clay Grain Coats (DCGC) with partial clay drapes, aggregates or bridges between grains (arrows; from facies F3). C) Coat (outline in red) with pyrite embedded within clay minerals (from facies F3). D) Same picture taken with reflected light device highlighting the framboidal pyrite embedded within the detrital clay grain coat. E) SEM picture showing aggregates at the surface of a quartz grain forming detrital clay grain coats (from facies F5a). F) Zoom of picture E on an aggregate showing a diatom embedded within clay minerals. G) Bridge texture composed of clay minerals associated with other components such as silt-sized quartz grains (from facies F5a). H) Zoom from box number 1 in the bridge showing a mix of clay minerals and silts. I) Zoom from box number 2 showing a diatom on the quartz grain surface. ***2 columns fitting image***

**Figure 8:** Representative microphotographs under optical microscope and SEM showing grain composition and the textural characteristics of sand coats within the Richard tidal bar. A-B) Microphotographs showing quartz (Qz), Feldspars (Fd), lithic (Li) detrital grains including carbonated elements of holoturian spicules and probably echinoderms (Ec) and brown detrital clay minerals surrounding framework grains, showing aggregates or forming bridges between grains (arrows; from facies F3). C) Detrital clay grain coat with pyrites embedded within clay minerals (from facies F5b). D) Same picture taken with reflected light device highlighting the framboidal pyrites embedded within the detrital clay grain coat. E) Microphotograph showing on a same picture detrital clay grain coats formed by aggregates or partial clay drapes surrounding the grain including a diatom in the grain surface (from facies F5b). F) SEM pictures showing aggregated detrital clay grain coats at the surface of quartz grains covering a more or less large surface area (from facies F3). G) SEM pictures showing aggregated detrital clay grain coats at the surface of a quartz grain (from facies F5b). H-I) Zoom from box number 1 and 2 showing carbonated elements as coccoliths or diatoms skeleton embedded within clay minerals. ***2 columns fitting image***

**Figure 9:** Evolution of mean grain size, surface area of clay minerals from XRD semi-quantifications, coated grain content and FTIR measurements along the three cores of the Plassac tidal bar. Sand rich facies are in yellow while muddy facies are in grey. The surfaces area from the diffractograms were reduced to the percentage of fine fraction measured in the sample. LWST = Low Water of Spring Tides. ***2 columns fitting image***

**Figure 10:** Evolution of mean grain size, surface area of clay minerals from XRD semi-quantifications, coated grain content and FTIR measurements along the three cores of the Richard tidal bar. Sand rich facies are in yellow while muddy facies are in grey. The surfaces area from the diffractograms were reduced to the percentage of fine fraction measured in the sample. LWST = Low Water of Spring Tides. ***2 columns fitting image***

**Figure 11:** Average coated grain content per facies with coat coverage classes associated. The sum of the coat coverage classes gives the total coated grain content for each facies indicated above the histograms. ***2 columns fitting image***

**Figure 12:** A) X-Ray diffractogram showing clay minerals identifiable within the Plassac tidal bar with no treatment (red line) or after ethylene-glycol saturation (blue line). B) X-Ray diffractogram showing clay minerals identifiable within the Richard tidal bar with no treatment (purple line) or after ethylene-glycol saturation (green line). C) Infra-red (SWIR) spectra on some Plassac tidal bars samples. D) Results from TEM analysis and plotted in the M+-4Si-R2+. ***2 columns fitting image***

**Figure 13:** Plate illustrating some hydrodynamic parameters in the Gironde estuary that may influence facies deposition. A) Measurements at PK 55 in the area of the Trompeloup tidal bar near the estuary funnel bottom showing the Fluid Mud Zone (FMZ). Erosion preferentially occurs at mid-ebb and mid-flood, at high current velocities, whereas tidal slacks are periods of deposition. B) Seasonal movement of the FMZ along the estuary influenced by river discharge variations (modified from Allen et al., 1974). C) Tidal current

velocity model along a cross-section normal to the Plassac tidal bar and showing tidal current evolution with depth and along the two spits of the bar. ***2 columns fitting image***

**Figure 14:** A) Bathymetric digital elevation models of the Plassac tidal bar from 1963 to 1983, showing the seaward migration of sand bodies (mini flood lobes) and their merging with the eastern spit of the bar (modified from Chaumillon et al., 2013). B) Bathymetric evolution model of the Richard tidal bar computed after bathymetric maps analysis, showing the landward and westward migration from 1901 to 1968 followed by a seaward and eastward migration and extension of the bar from 1968 to 1996. The present-day location is based on aerian pictures from Google Earth. ***2 columns fitting image***

**Figure 15:** Mean river discharges per year from 1925 to 1996 in the Gironde estuary. Green bars indicate an overall period of low-river discharges ***2 columns fitting image***

**Figure 16:** Large scale to small scale reservoir models of the two tidal bars. Location in the estuary, diagram from an aerial point of view of the bars, cross-section within the bars showing schematically the internal architecture of the reservoir units, vertical association of synthetic facies with representative core sections and microscopic pictures of the best reservoir facies with coatings associated with detrital grains. The best reservoir geobody is located in the outer estuary in the Richard tidal bar with two superimposed sand units separated by a single clay layer discontinuity. Abbreviations mean: Qz: Quartz, Li: Lithic grains, Fd: Feldspar, Mu: Muscovite, Bc: Bioclast, Ech: Echinoderm, G: Gastropod. ***2 columns fitting image***

**Table 1:** Table of facies recognized within tidal bars

**Table 2:** Table of data with mean values per facies and per tidal bars. Clay minerals semi quantification was only realized on samples analyzed through XRD (first column of clay fraction), but the real clay fraction for each facies was determined on more samples (second column of clay fraction).

## Supplementary material

**Appendix S1:** Detailed description of material and methods

**Figure S1:** Correlation between CEC analysis and FTIR parameters (water band and AL2OH+2253 nm adsorption bands)

**Appendix S2:** Data table per tidal bar showing results from semi-quantifications on thin sections.

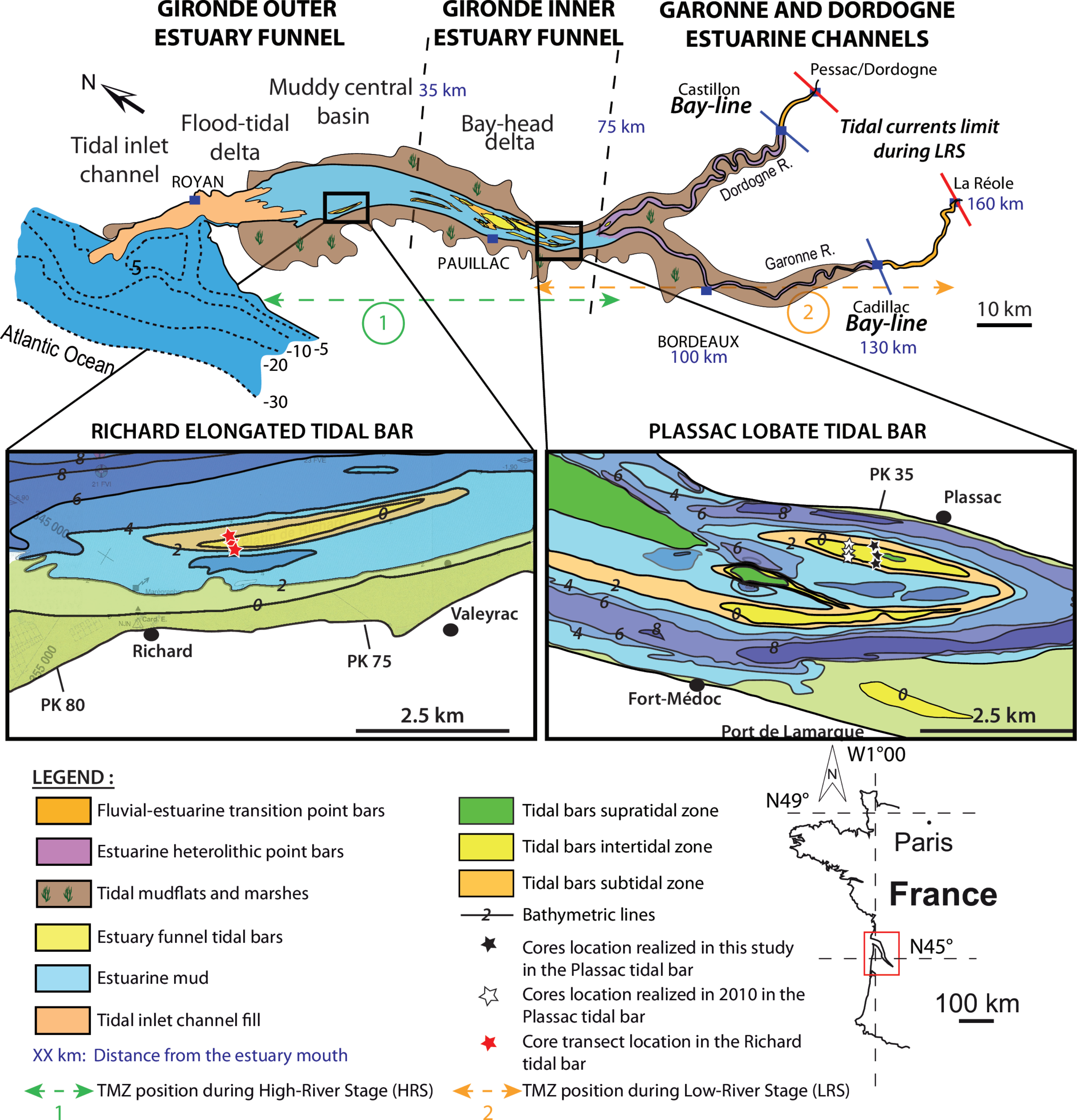
GIRONDE OUTER ESTUARY FUNNEL
GIRONDE INNER ESTUARY FUNNEL
GARONNE AND DORDOGNE ESTUARINE CHANNELS
N
Muddy central basin
35 km
Flood-tidal delta
Tidal inlet channel
ROYAN
Bay-head delta
75 km
Castillon
Bay-line
Pessac/Dordogne
Tidal currents limit during LRS
Dordogne R.
La Réole
160 km
Garonne R.
PAUILLAC
Cadillac
Bay-line
130 km
BORDEAUX
100 km
10 km
1
2
Atlantic Ocean
-5
-10
-5
-20
-30
RICHARD ELONGATED TIDAL BAR
PLASSAC LOBATE TIDAL BAR
8
6
4
2
0
Richard
Valeyrac
PK 75
PK 80
2.5 km
PK 35
Plassac
Fort-Médoc
Port de Lamarque
2.5 km
W1°00
N
N49°
Paris
France
N45°
100 km
LEGEND :
Fluvial-estuarine transition point bars
Estuarine heterolithic point bars
Tidal mudflats and marshes
Estuary funnel tidal bars
Estuarine mud
Tidal inlet channel fill
XX km: Distance from the estuary mouth
Tidal bars supratidal zone
Tidal bars intertidal zone
Tidal bars subtidal zone
Bathymetric lines
Cores location realized in this study in the Plassac tidal bar
Cores location realized in 2010 in the Plassac tidal bar
Core transect location in the Richard tidal bar
TMZ position during High-River Stage (HRS)
TMZ position during Low-River Stage (LRS)

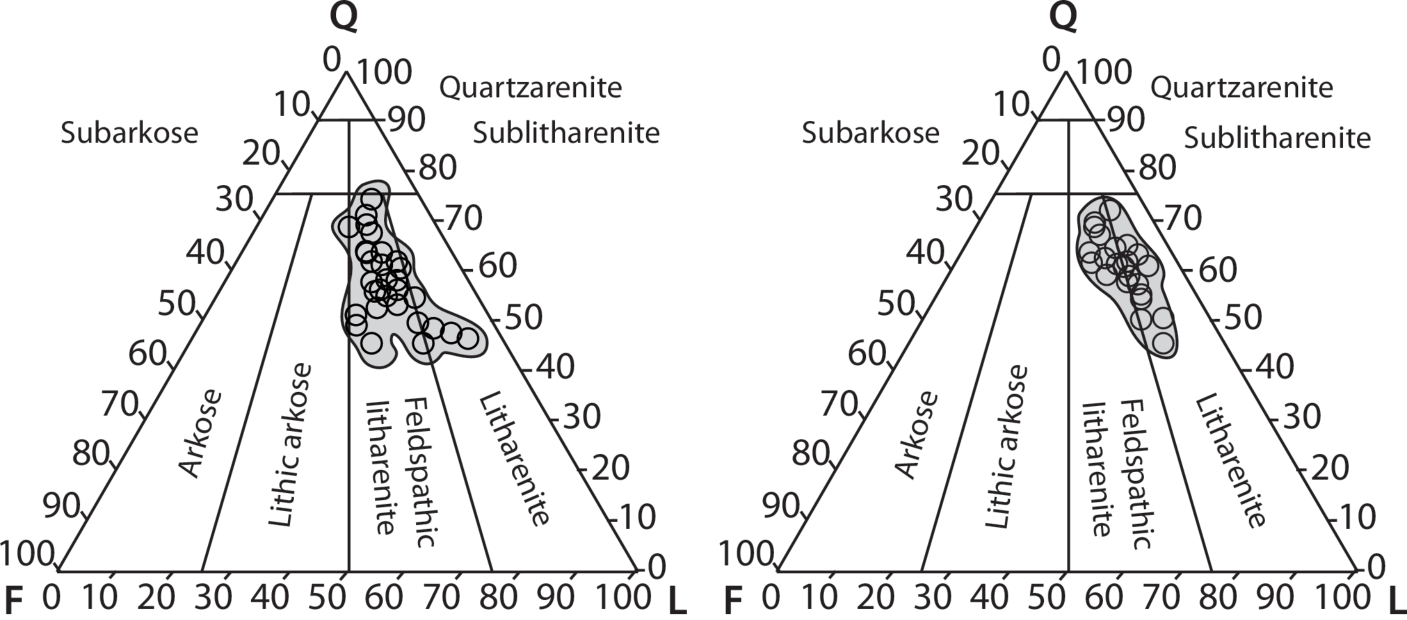

Plassac cores

Richard cores

# PLASSAC INNER ESTUARY FUNNEL TIDAL BAR

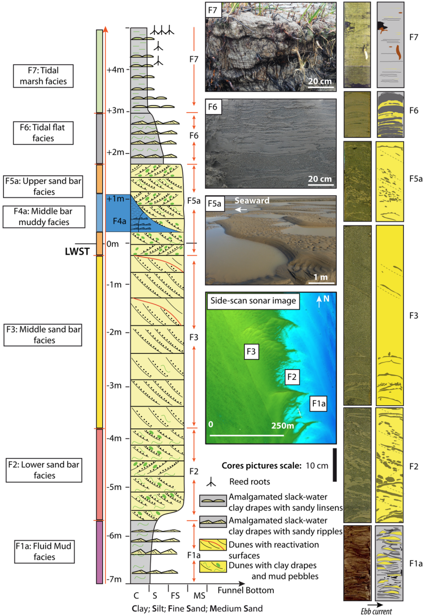

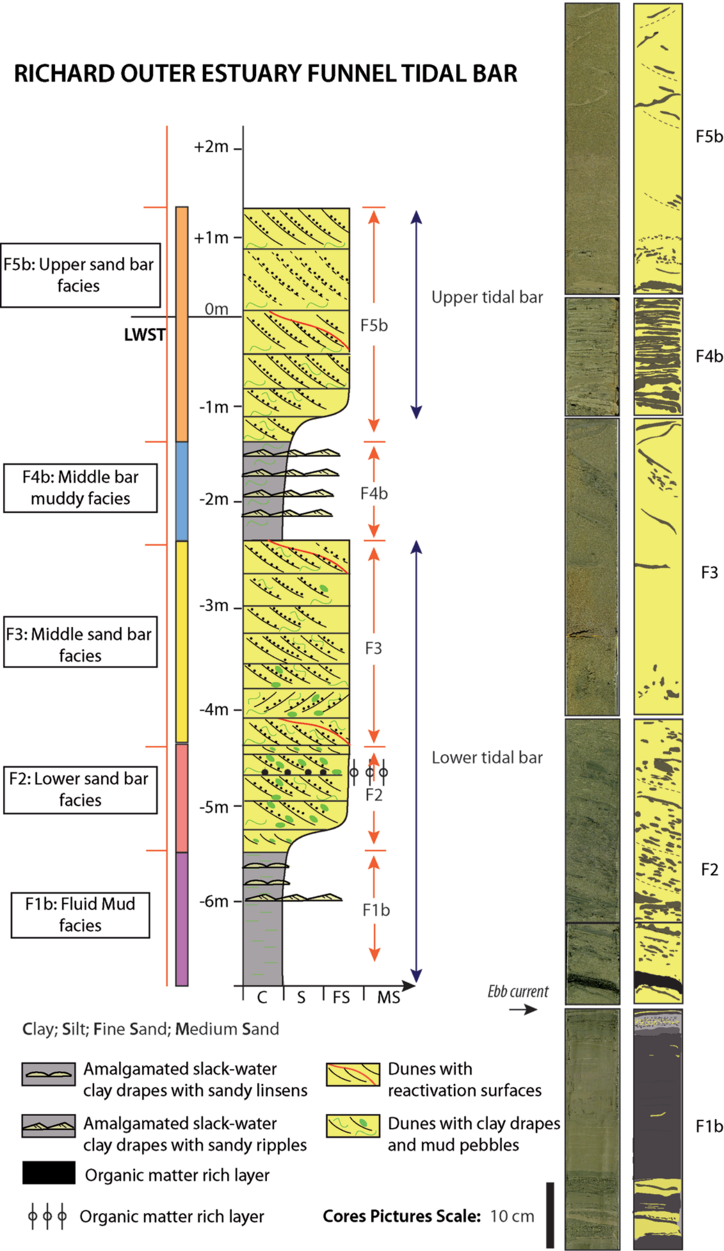
RICHARD OUTER ESTUARY FUNNEL TIDAL BAR
+2m
+1m
0m
LWST
-1m
-2m
-3m
-4m
-5m
-6m
F5b: Upper sand bar facies
F4b: Middle bar muddy facies
F3: Middle sand bar facies
F2: Lower sand bar facies
F1b: Fluid Mud facies
F5b
F4b
F3
F2
F1b
Upper tidal bar
Lower tidal bar
C
S
FS
MS
Clay; Silt; Fine Sand; Medium Sand
Amalgamated slack-water clay drapes with sandy linsens
Amalgamated slack-water clay drapes with sandy ripples
Organic matter rich layer
Organic matter rich layer
Dunes with reactivation surfaces
Dunes with clay drapes and mud pebbles
Cores Pictures Scale: 10 cm
Ebb current
F5b
F4b
F3
F2
F1b

**Plassac tidal bar cross-section**

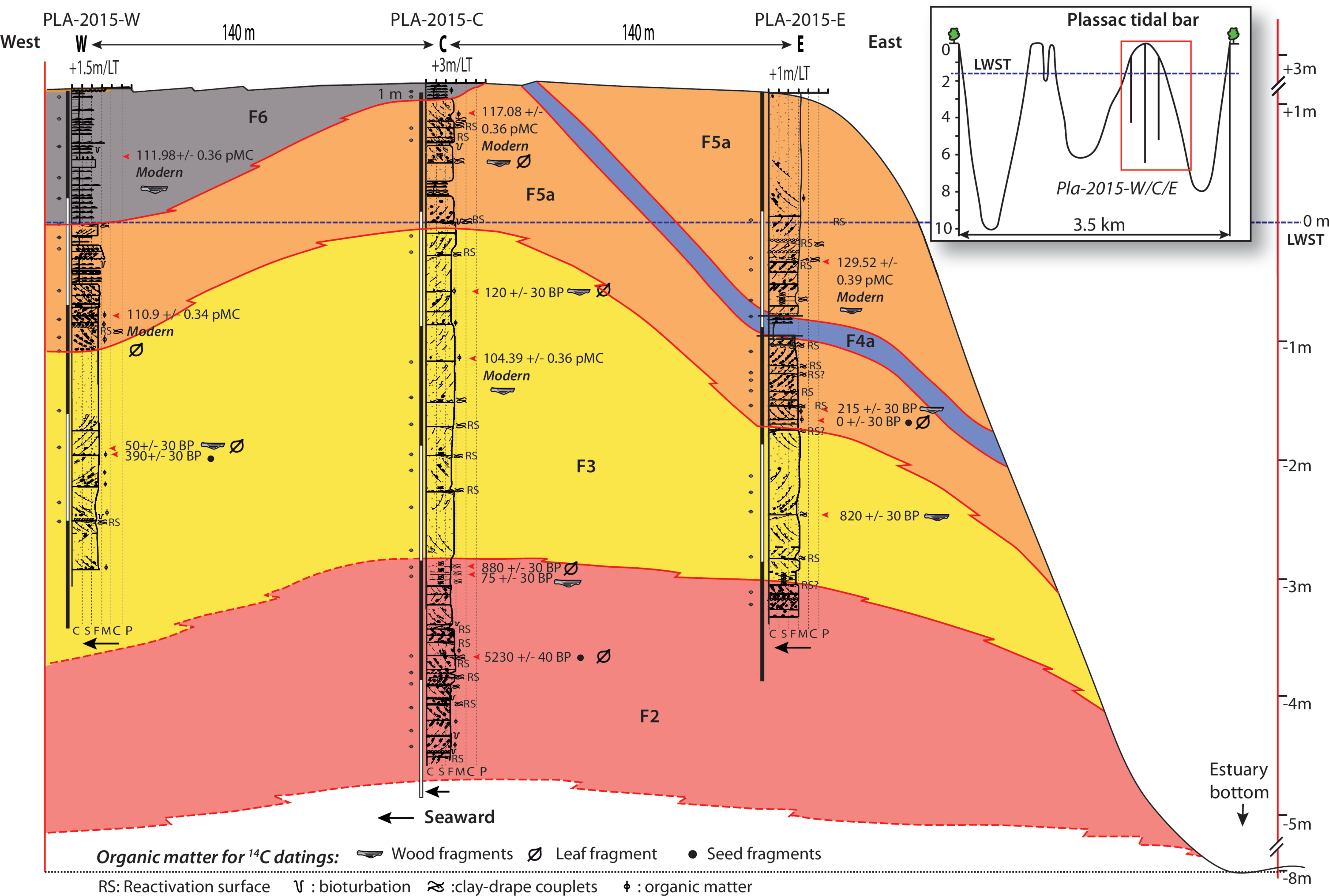

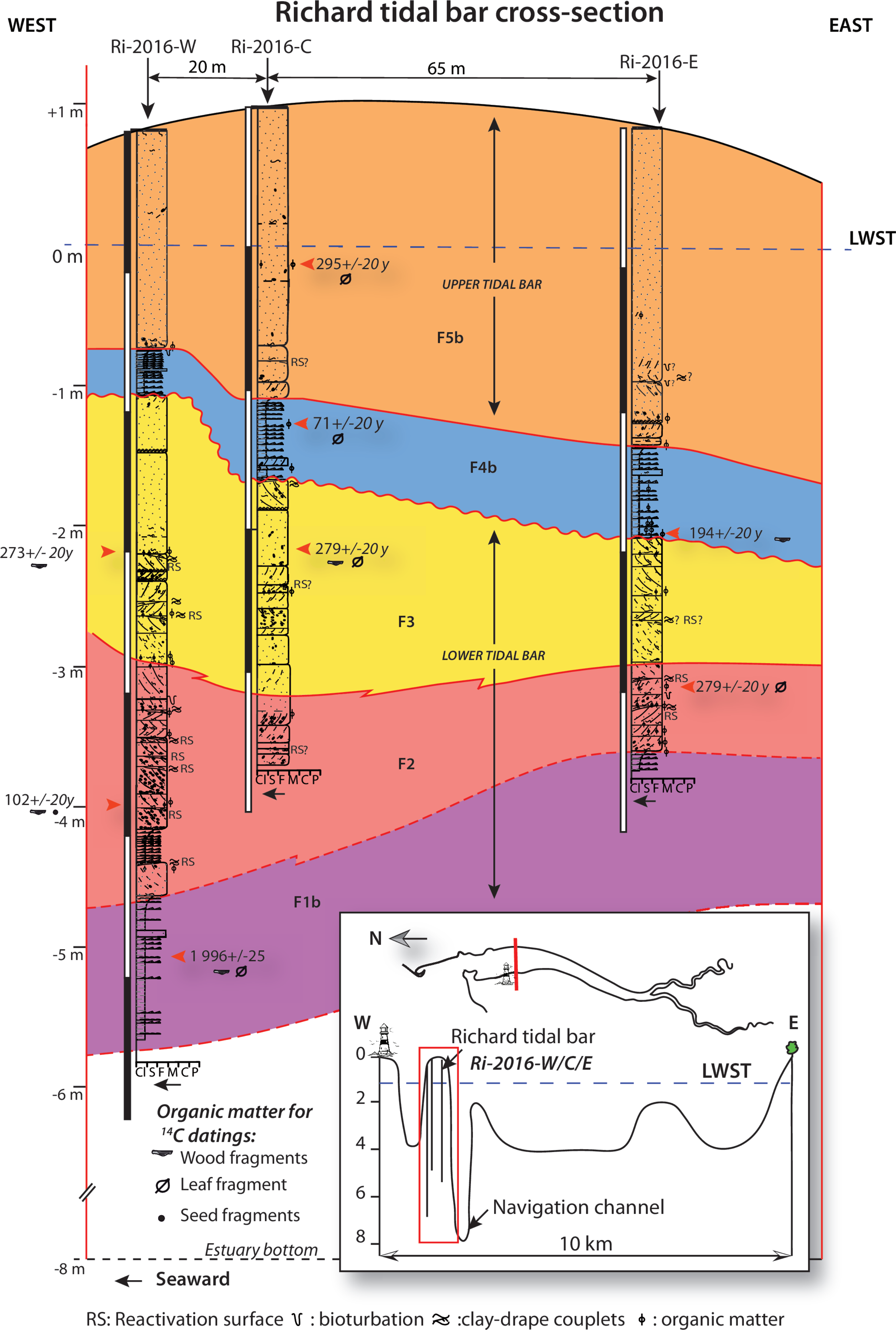
Richard tidal bar cross-section
WEST
EAST
Ri-2016-W
Ri-2016-C
Ri-2016-E
20 m
65 m
+1 m
0 m
-1 m
-2 m
-3 m
-4 m
-5 m
-6 m
-8 m
LWST
295+/-20 y
UPPER TIDAL BAR
F5b
RS?
71+/-20 y
F4b
194+/-20 y
273+/-20y
RS
279+/-20 y
F3
? RS?
LOWER TIDAL BAR
279+/-20 y
F2
102+/-20y
F1b
1 996+/-25
Cl S F M C P
Organic matter for $^{14}$C datings:
Wood fragments
Leaf fragment
Seed fragments
Estuary bottom
Seaward
N
W
E
Richard tidal bar
Ri-2016-W/C/E
LWST
0
2
4
6
8
Navigation channel
10 km
RS: Reactivation surface ∨ : bioturbation ≈ :clay-drape couplets ɸ : organic matter

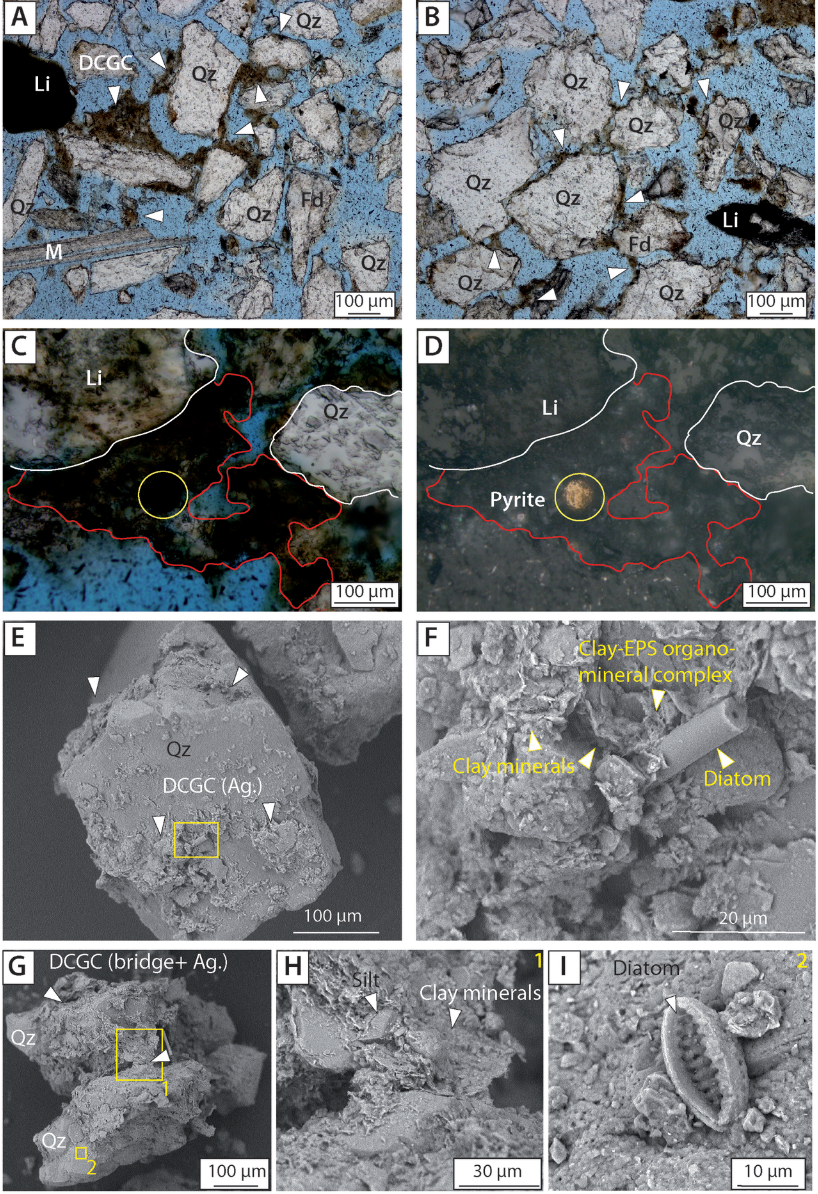
A
Qz
DCGC
Li
Qz
Qz
Qz
Fd
M
Qz
100 µm
B
Qz
Qz
Qz
Qz
Qz
Li
Fd
Qz
Qz
100 µm
C
Li
Qz
100 µm
D
Li
Qz
Pyrite
100 µm
E
Qz
DCGC (Ag.)
100 µm
F
Clay-EPS organo-mineral complex
Clay minerals
Diatom
20 µm
G
DCGC (bridge+ Ag.)
Qz
1
Qz
2
100 µm
H
1
Silt
Clay minerals
30 µm
I
Diatom
2
10 µm

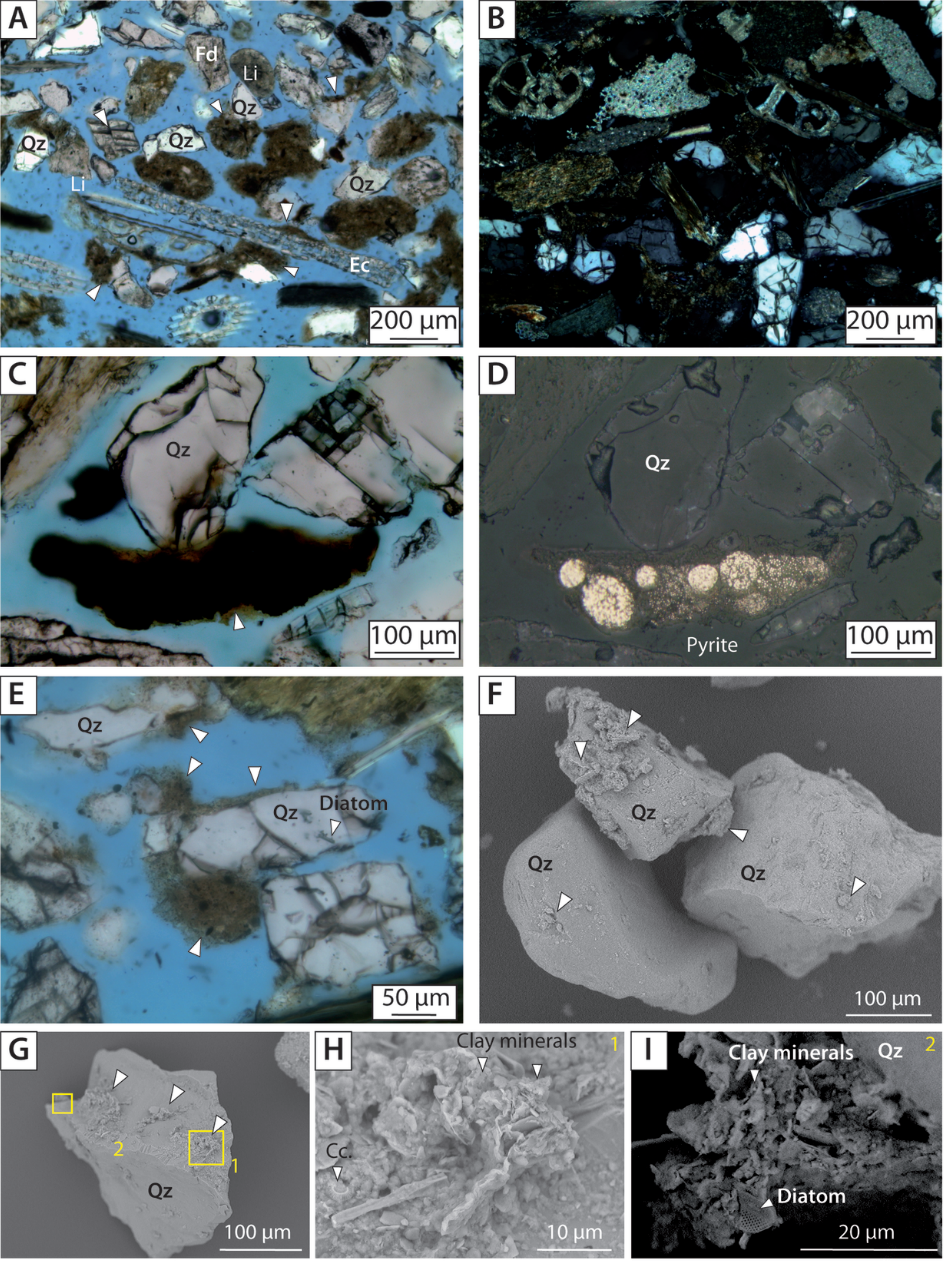
A
Fd
Li
Qz
Qz
Qz
Li
Qz
Ec
200 µm
B
200 µm
C
Qz
100 µm
D
Qz
Pyrite
100 µm
E
Qz
Qz
Diatom
50 µm
F
Qz
Qz
Qz
100 µm
G
2
1
Qz
100 µm
H
Clay minerals
1
Cc.
10 µm
I
Clay minerals
Qz
2
Diatom
20 µm

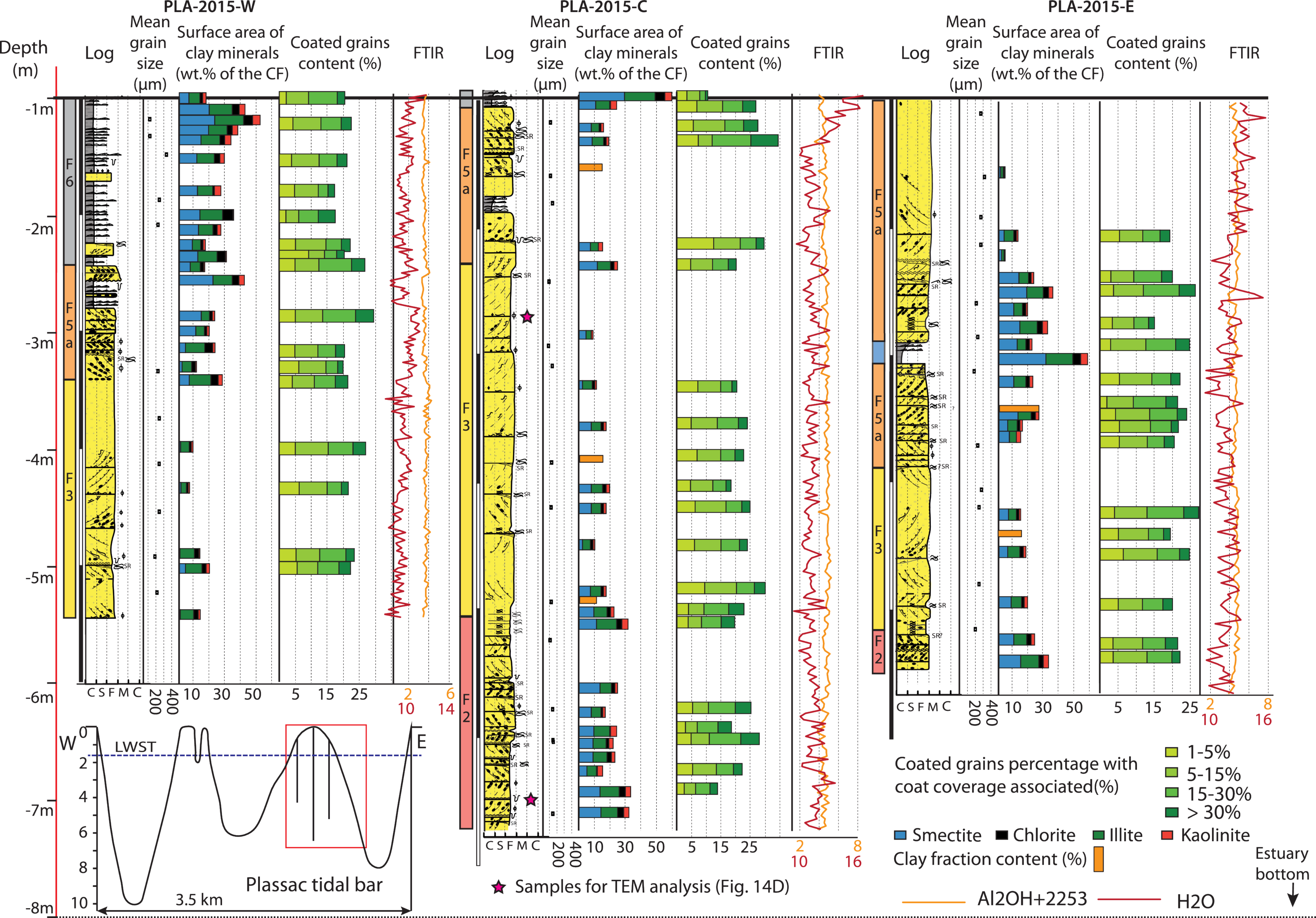
PLA-2015-W
PLA-2015-C
PLA-2015-E
Depth (m)
Log
Mean grain size (µm)
Surface area of clay minerals (wt.% of the CF)
Coated grains content (%)
FTIR
-1m
-2m
-3m
-4m
-5m
-6m
-7m
-8m
F6
F5a
F3
F2
SR
C S F M C
200 400
10 30 50
5 15 25
2 6
10 14
2 8
10 16
W
E
LWST
0
2
4
6
8
10
3.5 km
Plassac tidal bar
Samples for TEM analysis (Fig. 14D)
Coated grains percentage with coat coverage associated(%)
1-5%
5-15%
15-30%
> 30%
Smectite
Chlorite
Illite
Kaolinite
Clay fraction content (%)
Al2OH+2253
H2O
Estuary bottom

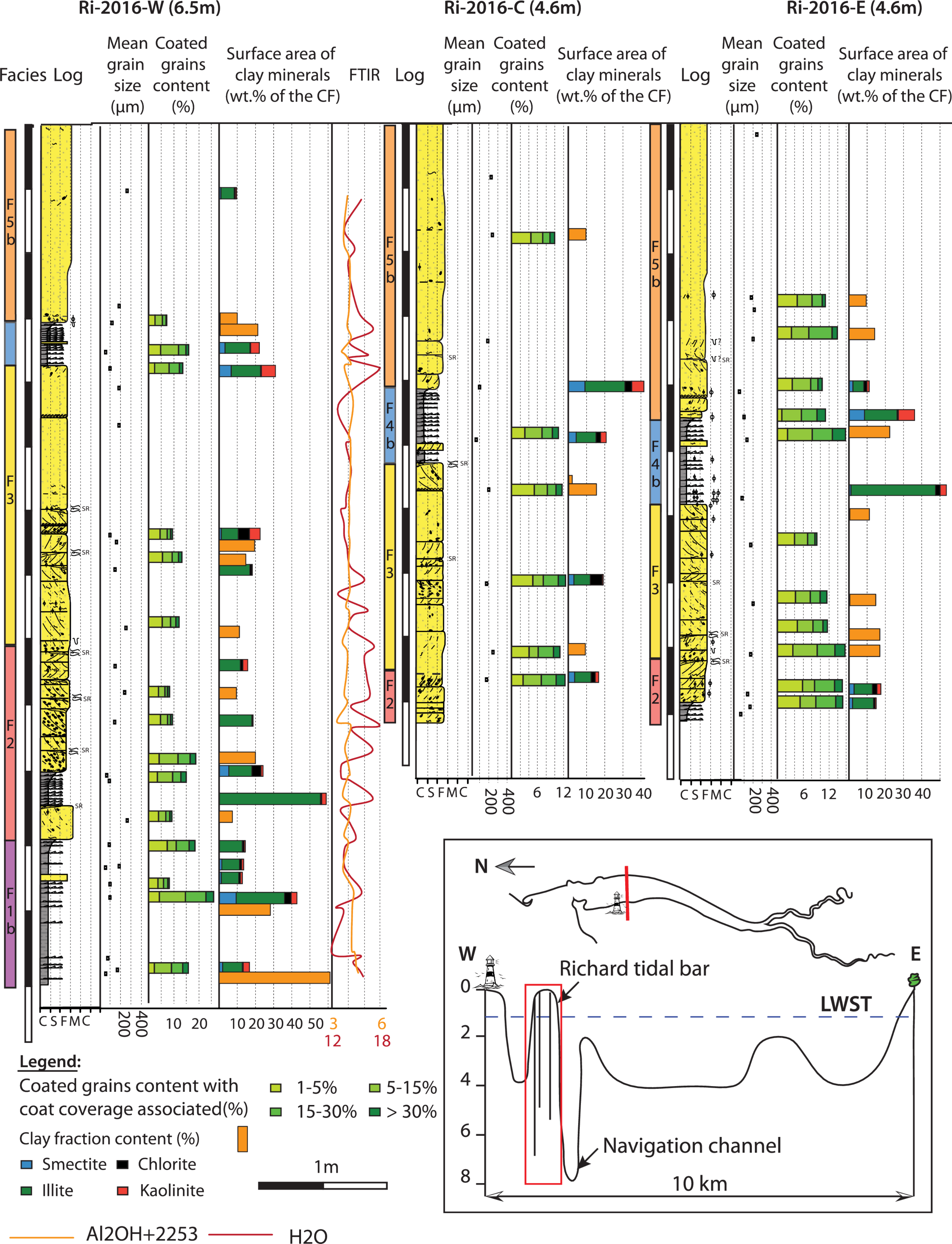
Ri-2016-W (6.5m)
Ri-2016-C (4.6m)
Ri-2016-E (4.6m)
Facies
Log
Mean grain size (µm)
Coated grains content (%)
Surface area of clay minerals (wt.% of the CF)
FTIR
F5b
F4b
F3
F2
F1b
SR
C S F M C
200
400
10
20
10 20 30 40 50
6
12
10 20 30 40
3
12
6
18
Legend:
Coated grains content with coat coverage associated(%)
1-5%
5-15%
15-30%
> 30%
Clay fraction content (%)
Smectite
Chlorite
Illite
Kaolinite
1m
Al2OH+2253
H2O
N
W
E
Richard tidal bar
LWST
Navigation channel
0
2
4
6
8
10 km

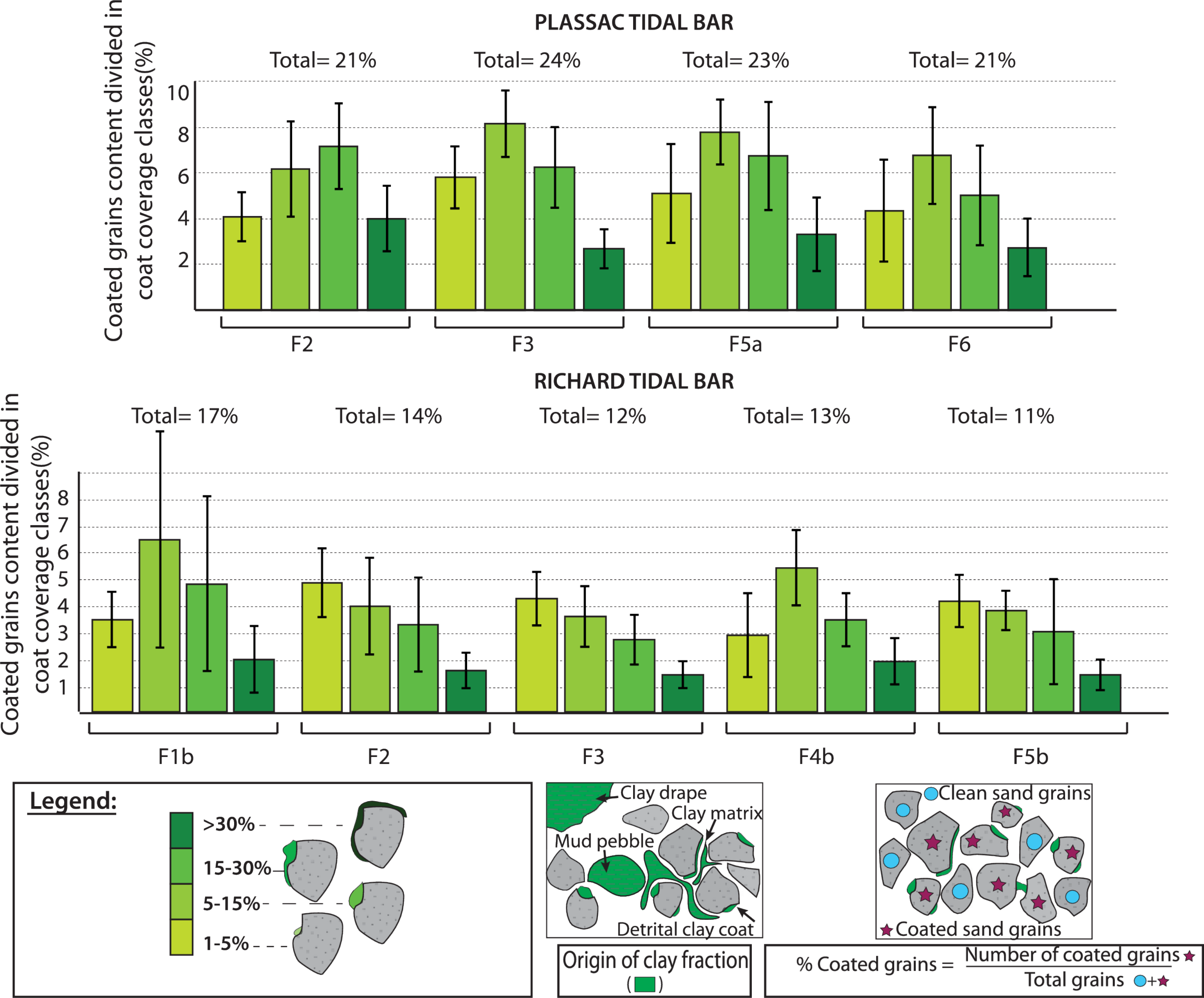
PLASSAC TIDAL BAR
Coated grains content divided in coat coverage classes(%)
Total= 21%
Total= 24%
Total= 23%
Total= 21%
10
8
6
4
2
F2
F3
F5a
F6
RICHARD TIDAL BAR
Coated grains content divided in coat coverage classes(%)
Total= 17%
Total= 14%
Total= 12%
Total= 13%
Total= 11%
8
7
6
5
4
3
2
1
F1b
F2
F3
F4b
F5b
Legend:
>30%
15-30%
5-15%
1-5%
Clay drape
Clay matrix
Mud pebble
Detrital clay coat
Origin of clay fraction
(🟩)
Clean sand grains
Coated sand grains
% Coated grains = Number of coated grains / Total grains

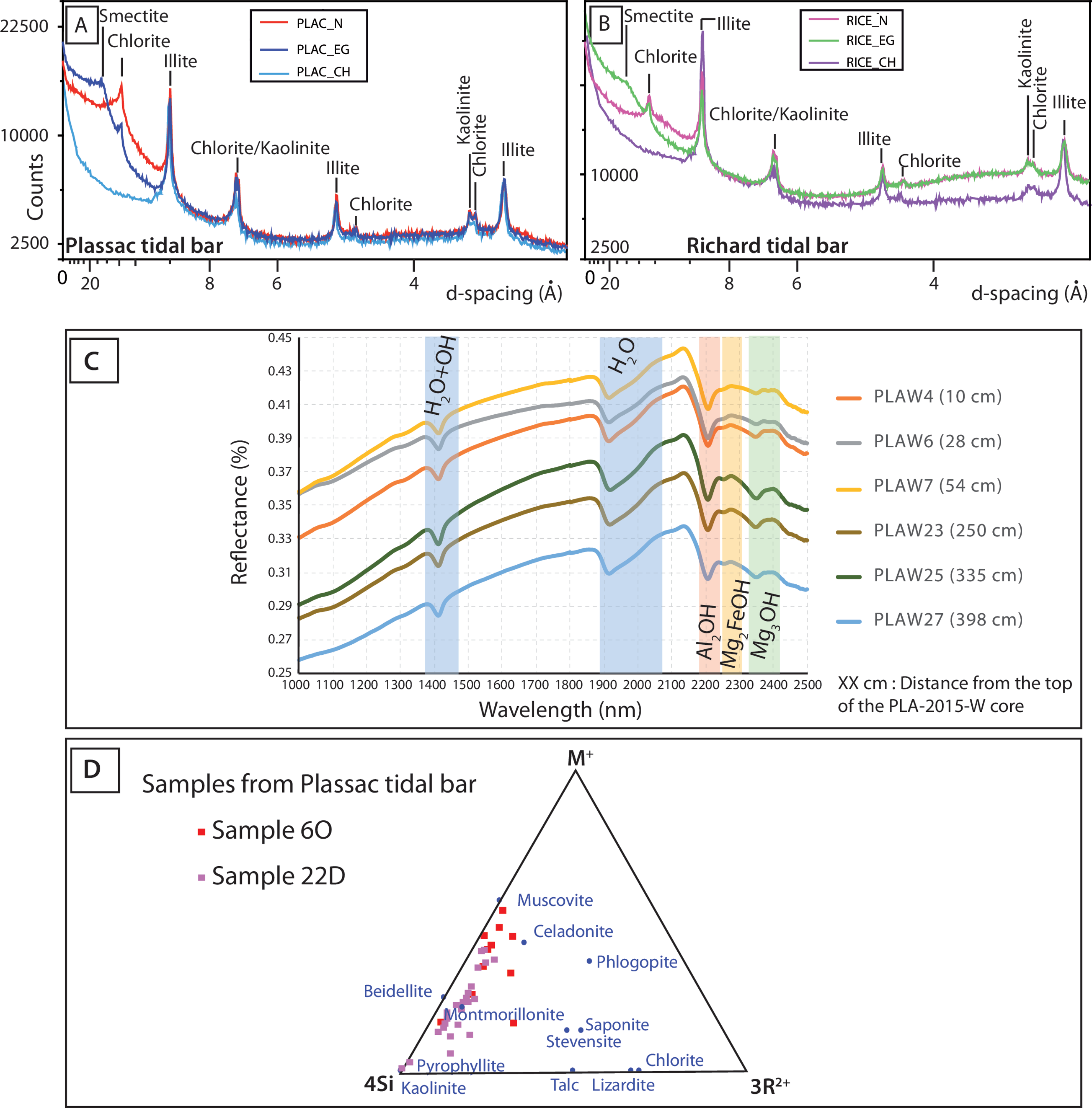
A
Smectite
Chlorite
Illite
Chlorite/Kaolinite
Illite
Chlorite
Kaolinite
Chlorite
Illite
PLAC_N
PLAC_EG
PLAC_CH
22500
10000
2500
Counts
Plassac tidal bar
0
20
8
6
4
d-spacing (Å)
B
Smectite
Illite
Chlorite
Chlorite/Kaolinite
Illite
Chlorite
Kaolinite
Chlorite
Illite
RICE_N
RICE_EG
RICE_CH
10000
2500
Richard tidal bar
0
20
8
6
4
d-spacing (Å)
C
H2O+OH
H2O
Al2OH
Mg2FeOH
Mg3OH
0.45
0.43
0.41
0.39
0.37
0.35
0.33
0.31
0.29
0.27
0.25
Reflectance (%)
1000 1100 1200 1300 1400 1500 1600 1700 1800 1900 2000 2100 2200 2300 2400 2500
Wavelength (nm)
PLAW4 (10 cm)
PLAW6 (28 cm)
PLAW7 (54 cm)
PLAW23 (250 cm)
PLAW25 (335 cm)
PLAW27 (398 cm)
XX cm : Distance from the top of the PLA-2015-W core
D
Samples from Plassac tidal bar
Sample 6O
Sample 22D
M+
4Si
3R2+
Muscovite
Celadonite
Phlogopite
Beidellite
Montmorillonite
Saponite
Stevensite
Pyrophyllite
Kaolinite
Talc
Lizardite
Chlorite

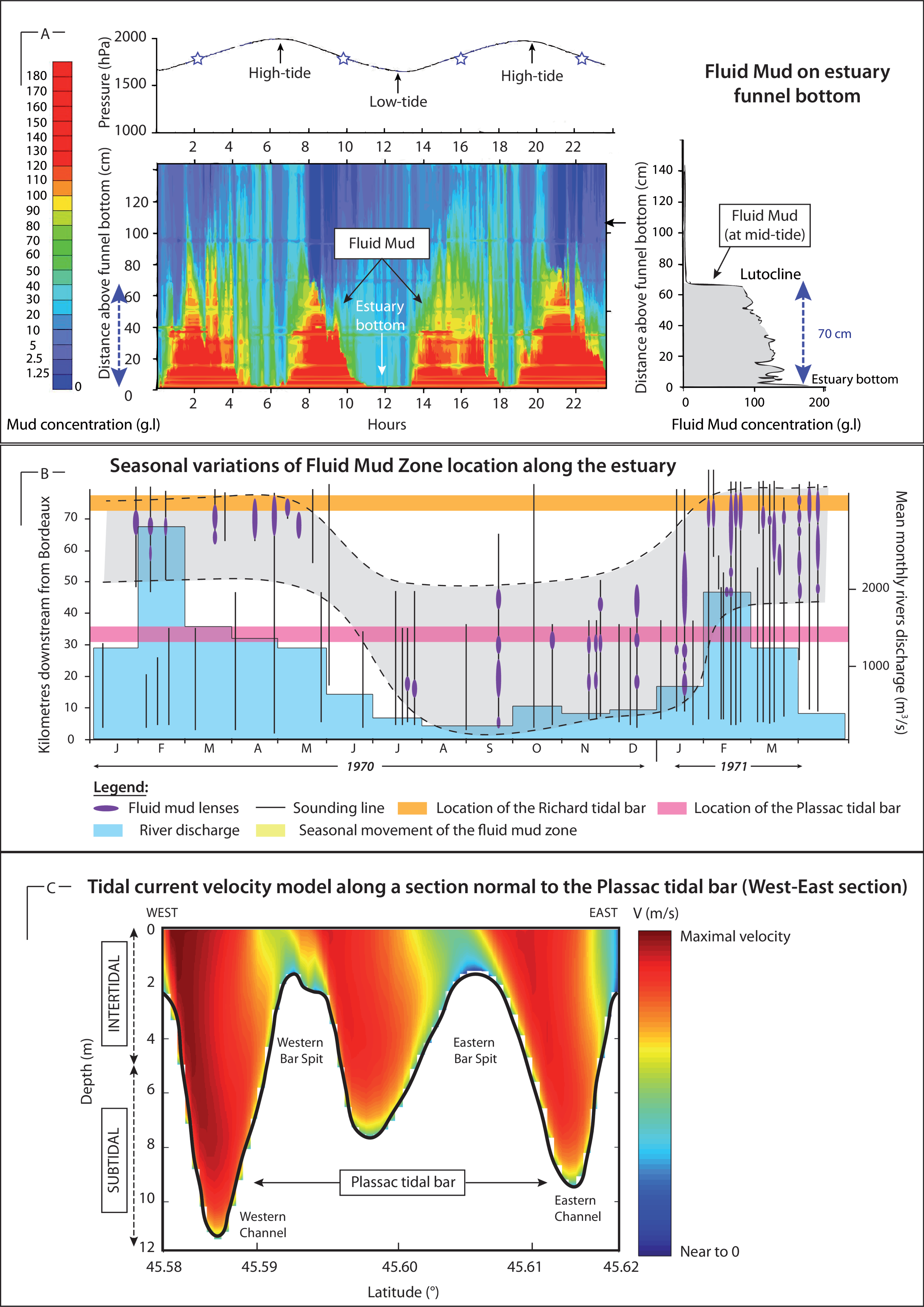
A
Fluid Mud on estuary funnel bottom
Pressure (hPa)
2000
1500
1000
High-tide
Low-tide
High-tide
2
4
6
8
10
12
14
16
18
20
22
180
170
160
150
140
130
120
110
100
90
80
70
60
50
40
30
20
10
5
2.5
1.25
0
Mud concentration (g.l)
Distance above funnel bottom (cm)
Fluid Mud
Estuary bottom
Hours
Fluid Mud (at mid-tide)
Lutocline
70 cm
Estuary bottom
Fluid Mud concentration (g.l)
B
Seasonal variations of Fluid Mud Zone location along the estuary
Kilometres downstream from Bordeaux
Mean monthly rivers discharge ($m^3/s$)
2000
1000
J
F
M
A
M
J
J
A
S
O
N
D
J
F
M
1970
1971
Legend:
Fluid mud lenses
Sounding line
Location of the Richard tidal bar
Location of the Plassac tidal bar
River discharge
Seasonal movement of the fluid mud zone
C
Tidal current velocity model along a section normal to the Plassac tidal bar (West-East section)
WEST
EAST
V (m/s)
Maximal velocity
Near to 0
Depth (m)
INTERTIDAL
SUBTIDAL
0
2
4
6
8
10
12
Western Bar Spit
Eastern Bar Spit
Plassac tidal bar
Western Channel
Eastern Channel
45.58
45.59
45.60
45.61
45.62
Latitude (°)

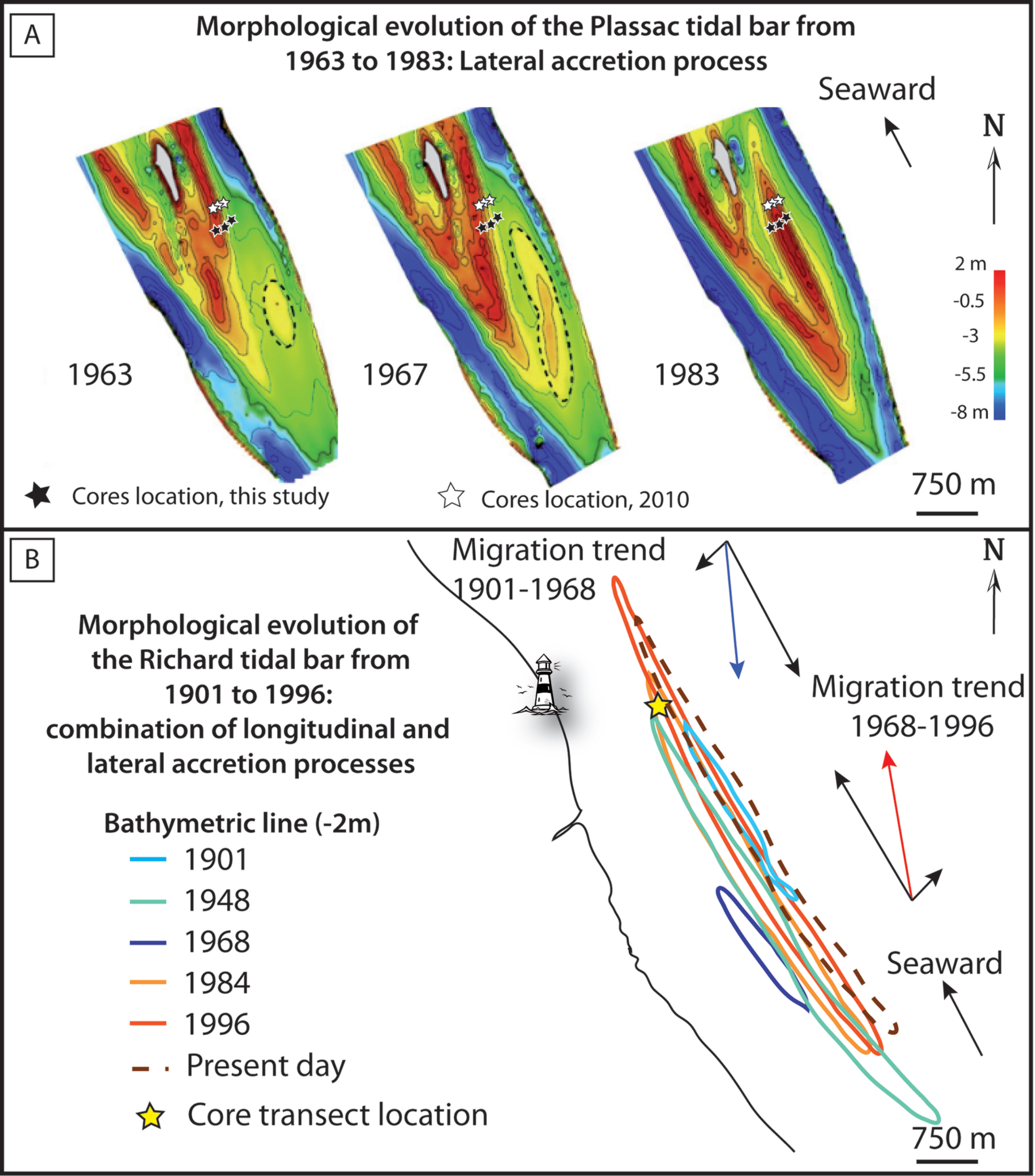
A
Morphological evolution of the Plassac tidal bar from 1963 to 1983: Lateral accretion process
Seaward
N
1963
1967
1983
2 m
-0.5
-3
-5.5
-8 m
750 m
★ Cores location, this study
☆ Cores location, 2010
B
Migration trend 1901-1968
N
Morphological evolution of the Richard tidal bar from 1901 to 1996: combination of longitudinal and lateral accretion processes
Migration trend 1968-1996
Bathymetric line (-2m)
1901
1948
1968
1984
1996
Present day
Seaward
★ Core transect location
750 m

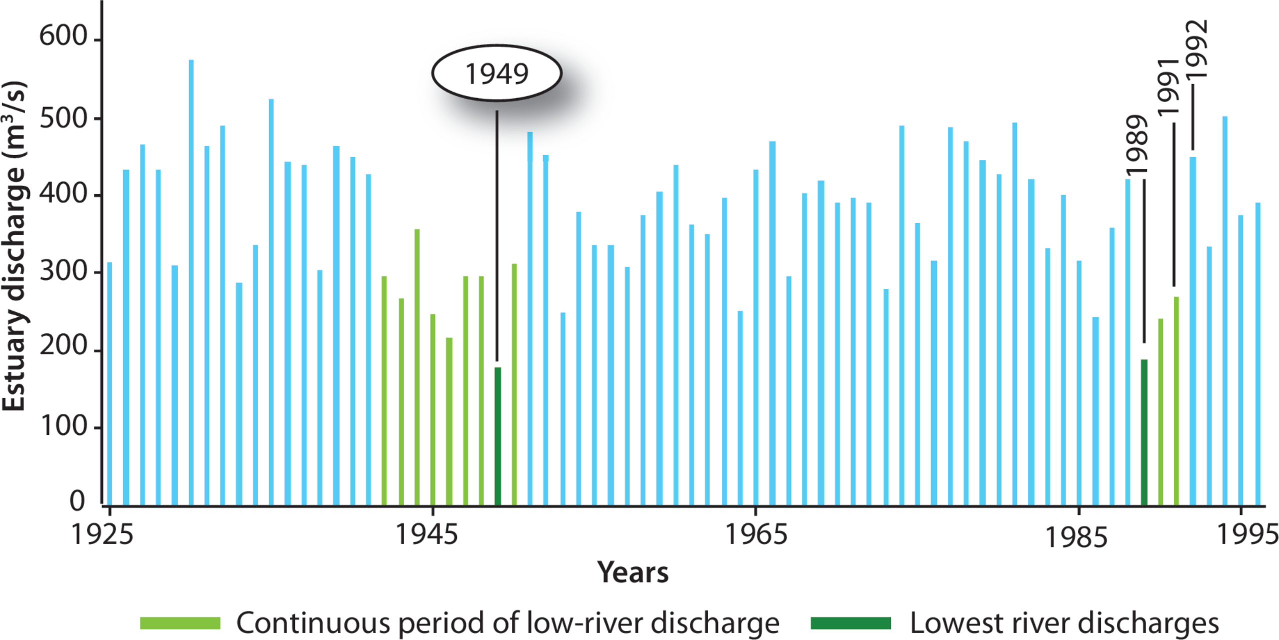
600
500
400
300
200
100
0
Estuary discharge (m³/s)
1949
1989
1991
1992
1925
1945
1965
1985
1995
Years
Continuous period of low-river discharge
Lowest river discharges

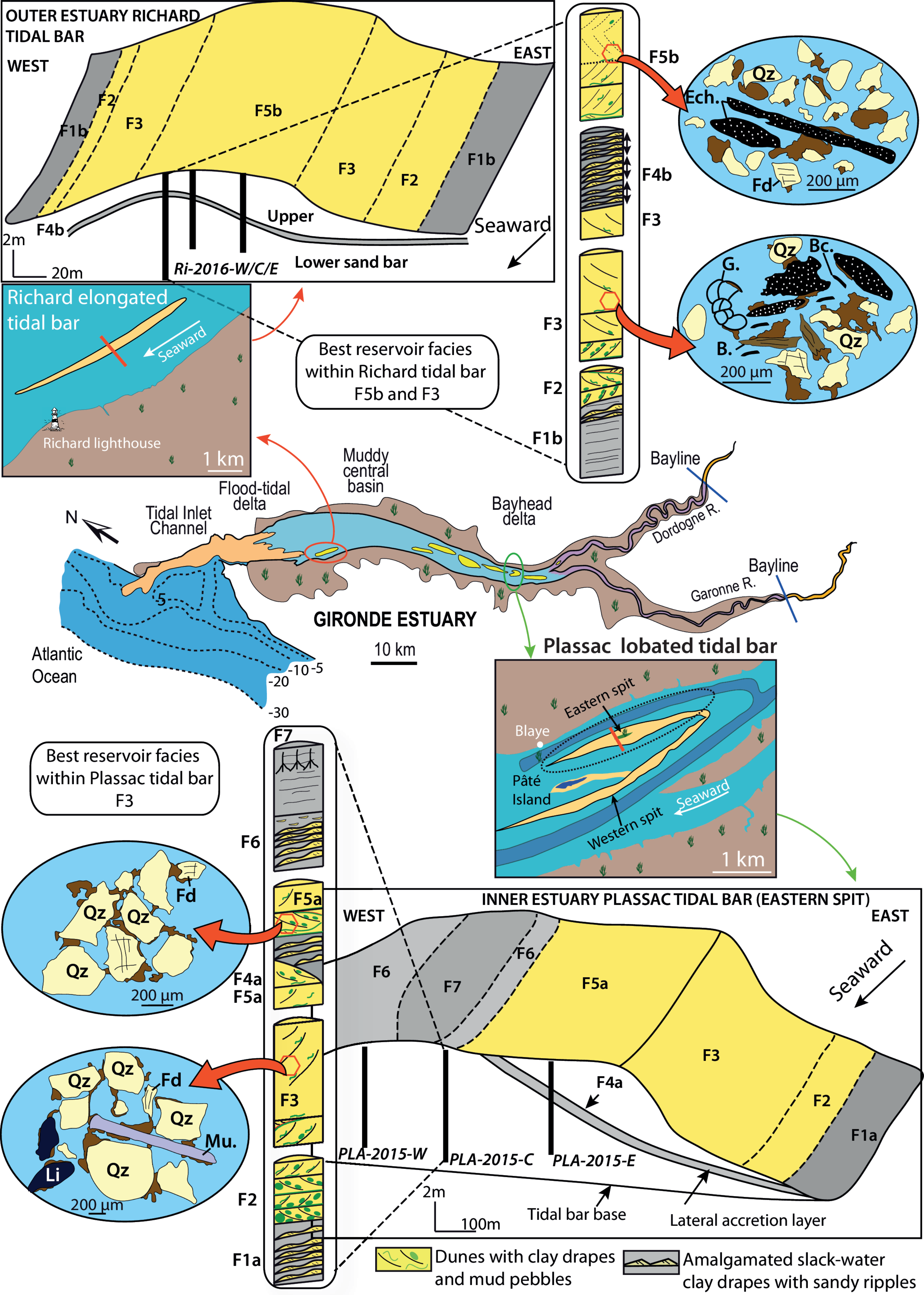
OUTER ESTUARY RICHARD TIDAL BAR
WEST
EAST
F1b
F2
F3
F5b
F3
F2
F1b
F4b
Upper
Lower sand bar
Seaward
2m
20m
Ri-2016-W/C/E
F5b
F4b
F3
F3
F2
F1b
Qz
Ech.
Fd
200 µm
Qz
Bc.
G.
B.
Qz
200 µm
Richard elongated tidal bar
Seaward
Richard lighthouse
1 km
Best reservoir facies within Richard tidal bar F5b and F3
Muddy central basin
Flood-tidal delta
Tidal Inlet Channel
N
Bayhead delta
Bayline
Dordogne R.
Bayline
Garonne R.
5
Atlantic Ocean
GIRONDE ESTUARY
10 km
-5
-10
-20
-30
Plassac lobated tidal bar
Eastern spit
Blaye
Pâté Island
Western spit
Seaward
1 km
Best reservoir facies within Plassac tidal bar F3
F7
F6
F5a
F4a
F5a
F3
F2
F1a
Fd
Qz
Qz
Qz
200 µm
Qz
Qz
Fd
Qz
Mu.
Li
Qz
200 µm
INNER ESTUARY PLASSAC TIDAL BAR (EASTERN SPIT)
WEST
EAST
F6
F7
F6
F5a
F3
F2
F1a
F4a
Seaward
PLA-2015-W
PLA-2015-C
PLA-2015-E
2m
100m
Tidal bar base
Lateral accretion layer
Dunes with clay drapes and mud pebbles
Amalgamated slack-water clay drapes with sandy ripples

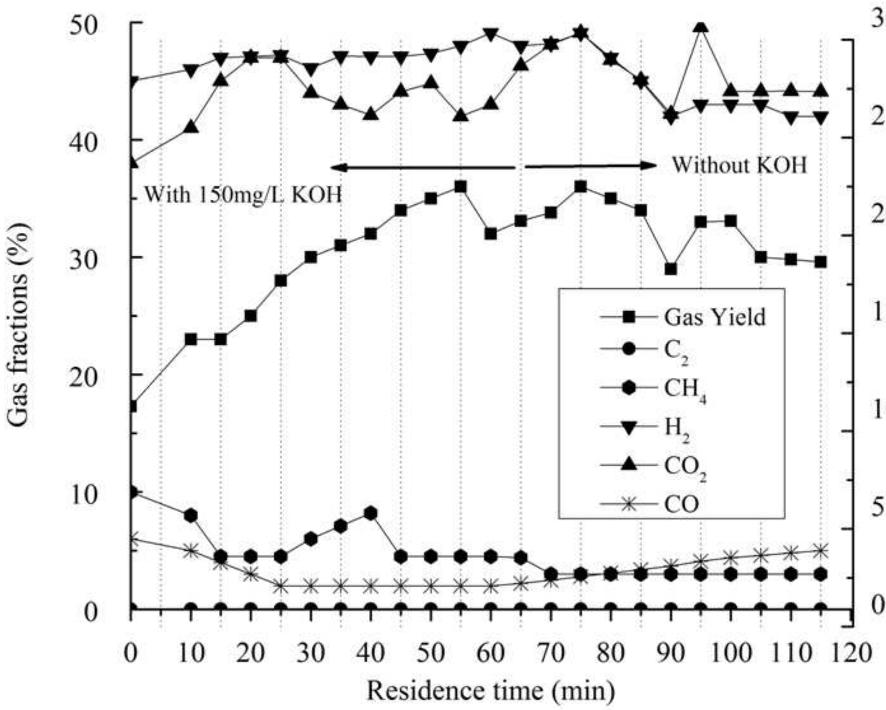

**Fig.4 The composition and total yield of the gas product from SCWG of coking wastewater with 150 mg/L KOH and without KOH (540°C, 25 MPa).**

|  | Facies number | Coated grain content divided according to the different coat |  |  |  |  |  | Porosity (%) | Mean grain size (µm) | Clay minerals (reduced to the percentage of clay |  |  |  |  | Clay fraction (wt%) from XRD samples | Total clay fraction (all samples) (wt%) |
|---|---|---|---|---|---|---|---|---|---|---|---|---|---|---|---|---|
|  |  | **Number of samples** | **1-5%** | **5-15%** | **15-30%** | **> 30%** | **Total coated grain content** |  |  | **Number of samples** | **Smectite** | **Illite** | **Chlorite** | **Kaolinite** |  |  |
| **Plassac tidal bar** | F6 | 8 | 4 | 7 | 5 | 3 | 19 | 25 | 208 | 12 | 15 | 12 | 4 | 3 | 34 | 34 |
|  | F5a | 20 | 5 | 8 | 7 | 4 | 24 | 25 | 237 | 25 | 9 | 7 | 2 | 2 | 20 | 20 |
|  | F4a | / | / | / | / | / | / | / | / | 1 | 31 | 17 | 5 | 5 | 58 | 58 |
|  | F3 | 16 | 6 | 8 | 6 | 3 | 23 | 26 | 224 | 20 | 5 | 7 | 2 | 2 | 15 | 15 |
|  | F2 | 8 | 4 | 6 | 7 | 4 | 21 | 25 | 231 | 12 | 11 | 9 | 2 | 3 | 26 | 25 |
| **Average Plassac** |  | **∑=52** | **5** | **7** | **6** | **3** | **22** | **25** | **225** | **∑=70** | **14** | **11** | **3** | **3** | **31** | **30** |
| **Richard tidal bar** | F5b | 5 | 4 | 3 | 3 | 1 | 11 | 35 | 178 | 10 | 3 | 10 | 1 | 3 | 17 | 17 |
|  | F4b | 4 | 3 | 5 | 3 | 2 | 13 | 33 | 99 | 4 | 5 | 23 | 2 | 5 | 35 | 37 |
|  | F3 | 12 | 4 | 4 | 3 | 1 | 12 | 38 | 182 | 12 | 3 | 13 | 4 | 4 | 23 | 14 |
|  | F2 | 8 | 5 | 4 | 3 | 2 | 14 | 34 | 166 | 10 | 2 | 20 | 2 | 2 | 25 | 21 |
|  | F1b | 3 | 3 | 6 | 5 | 2 | 17 | 31 | 138 | 6 | 4 | 14 | 2 | 2 | 21 | 29 |
| **Average Richard** |  | **∑=32** | **4** | **5** | **3** | **2** | **13** | **34** | **153** | **∑=42** | **3** | **16** | **2** | **3** | **24** | **24** |